Angewandte Chemie
Eine Zeitschrift der Gesellschaft Deutscher Chemiker

Supporting Information

Snapshots of a Migrating H-Atom: Characterization of a Reactive Iron(III) Indenide Hydride and its Nearly Isoenergetic Ring-Protonated Iron(I) Isomer

*Marcus W. Drover, Dirk J. Schild, Paul H. Oyala, and Jonas C. Peters**

anie_201909050_sm_miscellaneous_information.pdf

Table of Contents:

I. General Considerations:

All experiments were carried out employing standard Schlenk techniques under an atmosphere of dry nitrogen employing degassed, dried solvents in a solvent purification system supplied by SG Water, LLC. Non-halogenated solvents were tested with a standard purple solution of sodium benzophenone ketyl in tetrahydrofuran in order to confirm effective moisture removal. *trans*-$FeBr_2(depe)_2$[1], $FeBr_2(dippe)$[2], Fe(η^6-toluene)(dippe),[3] Fe(Cp*)(dppe)H[4] were prepared according to a literature procedure. All other reagents were purchased from commercial vendors and used without further purification unless otherwise stated.

***Hydrogen Analysis*:** The headspace of reaction flasks was analyzed by gas chromatography to quantify H_2 evolution with an Agilent 7890A gas chromatograph (HPPLOT U, 30 m, 0.32 mm i.d., 30 °C isothermal, 1 mL/min flow rate, N_2 carrier gas) using a thermal conductivity detector.

II. Nuclear Magnetic Resonance Spectroscopy:

^1H and ^{13}C chemical shifts are reported in ppm relative to tetramethylsilane, using residual solvent resonances as internal standards. ^{31}P chemical shifts are reported in ppm and referenced externally to 85% aqueous H_3PO_4 at 0 ppm.

III. ^{57}Fe Mössbauer Spectroscopy:

Mössbauer spectra were recorded on a spectrometer from SEE Co. (Edina, MN) operating in the constant acceleration mode in transmission geometry. The sample was kept in an SVT-400 cryostat form Janis (Wilmington, MA), using liquid N_2 as a cryogen for 80 K measurements. The quoted isomer shifts are relative to the centroid of the spectrum of a metallic foil of α-Fe at room temperature. Solid samples were prepared by grinding solid material into a fine powder and then mounted in to a Delrin cup fitted with a screw cap as a boron nitride pellet. Solution samples were transferred to a sample cup and chilled to 77 K inside of the glovebox, and quickly removed from the glovebox and immersed in liquid N_2 until mounted in the cryostat. Data analysis was performed using WMOSS version 4 (www.wmoss.org) and quadrupole doublets were fit to Lorentzian lineshapes.[5]

IV. Infrared Spectroscopy:

Solid and thin film IR measurements were obtained on a Bruker Alpha spectrometer equipped with a diamond ATR probe.

V. UV-VIS Spectroscopy:

UV-Visible spectroscopy measurements were collected with a Cary 50 UV-Vis spectrophotometer using a 1 cm two-window quartz cell.

VI. EPR Spectroscopy:

Continuous wave X-band EPR spectra were obtained on a Bruker EMX spectrometer using solutions prepared as frozen glasses in 2-MeTHF. Pulse EPR spectroscopy: All pulse X-band (9.4-9.7) EPR, electron nuclear double resonance (ENDOR), and hyperfine sublevel correlation spectroscopy (HYSCORE) experiments were acquired using a Bruker ELEXSYS E580 pulse EPR spectrometer. X-band ENDOR and HYSCORE experiments were performed using a Bruker MD-4 X-band ENDOR resonator. Temperature control was achieved using an ER 4118HV-CF5-L Flexline Cryogen-Free VT cryostat manufactured by ColdEdge equipped with an Oxford Instruments Mercury ITC temperature controller.

All pulse X-band ($\nu \approx$ 9.4-9.7 GHz) EPR and electron nuclear double resonance (ENDOR) experiments were aquired using a Bruker (Billerica, MA) ELEXSYS E580 pulse EPR spectrometer equipped with a Bruker MD-4 resonator. Temperature control was achieved using an ER 4118HV-CF5-L Flexline Cryogen-Free VT cryostat manufactured by ColdEdge (Allentown, PA) equipped with an Oxford Instruments Mercury ITC.

Pulse X-band ENDOR was acquired using the Davies pulse sequence ($\pi - T_{RF} - \pi_{RF} - T_{RF} - \pi/2 - \tau - \pi -$ echo), where T_{RF} is the delay between mw pulses and RF pulses, π_{RF} is the length of the RF pulse and the RF frequency is randomly sampled during each pulse sequence.

X-band HYSCORE spectra were acquired using the 4-pulse sequence ($\pi/2 - \tau - \pi/2 - t_1 - \pi - t_2 - \pi/2 -$ echo), where τ is a fixed delay, while t_1 and t_2 are independently incremented by Δt_1 and Δt_2, respectively. The time domain data was baseline-corrected (third-order polynomial) to eliminate the exponential decay in the echo intensity, apodized with a Hamming window function, zero-filled to eight-fold points, and fast Fourier-transformed to yield the 2-dimensional frequency domain. For ^{2}H-^{1}H difference spectra, the time domain of the HYSCORE spectrum of the ^{1}H sample was subtracted from that of the ^{2}H sample, and the same data processing procedure detailed above was used to generate the frequency spectrum.

In general, the ENDOR spectrum for a given nucleus with spin I= ½ (^{1}H, ^{31}P) coupled to the S = ½ electron spin exhibits a doublet at frequencies

$$\nu_{\pm} = \left|\frac{A}{2} \pm \nu_N\right| \quad (1)$$

Where ν_N is the nuclear Larmor frequency and A is the hyperfine coupling. For nuclei with $I \geq 1$ (^{2}H), an additonal splitting of the $\nu_{\pm}$ manifolds is produced by the nuclear quadrupole interaction (P)

$$\nu_{\pm,m_I} = \left|\nu_N \pm \frac{3P(2m_I - 1)}{2}\right| \quad (2)$$

In HYSCORE spectra, these signals manifest as cross-peaks or ridges in the 2-D frequency spectrum which are generally symmetric about the diagonal of a given quadrant. This technique

allows hyperfine levels corresponding to the same electron-nuclear submanifold to be differentiated, as well as separating features from hyperfine couplings in the weak-coupling regime ($|A| < 2|\nu_I|$) in the (+,+) quadrant from those in the strong coupling regime ($|A| > 2|\nu_I|$) in the (−,+) quadrant. The (−,−) and (+,−) quadrants of these frequency spectra are symmetric to the (+,+) and (−,+) quadrants, thus typically only two of the quadrants are typically displayed in literature.

For systems with appreciable hyperfine anisotropy in frozen solutions or solids, HYSCORE spectra typically do not exhibit sharp cross peaks, but show ridges that represent the sum of cross peaks from selected orientations within the excitation bandwidth of the MW pulses at the magnetic field position at which the spectrum is collected. The length and curvature of these correlation ridges can allow for the separation and estimation of the magnitude of the isotropic and dipolar components of the hyperfine tensor, as shown in Fig. S1.

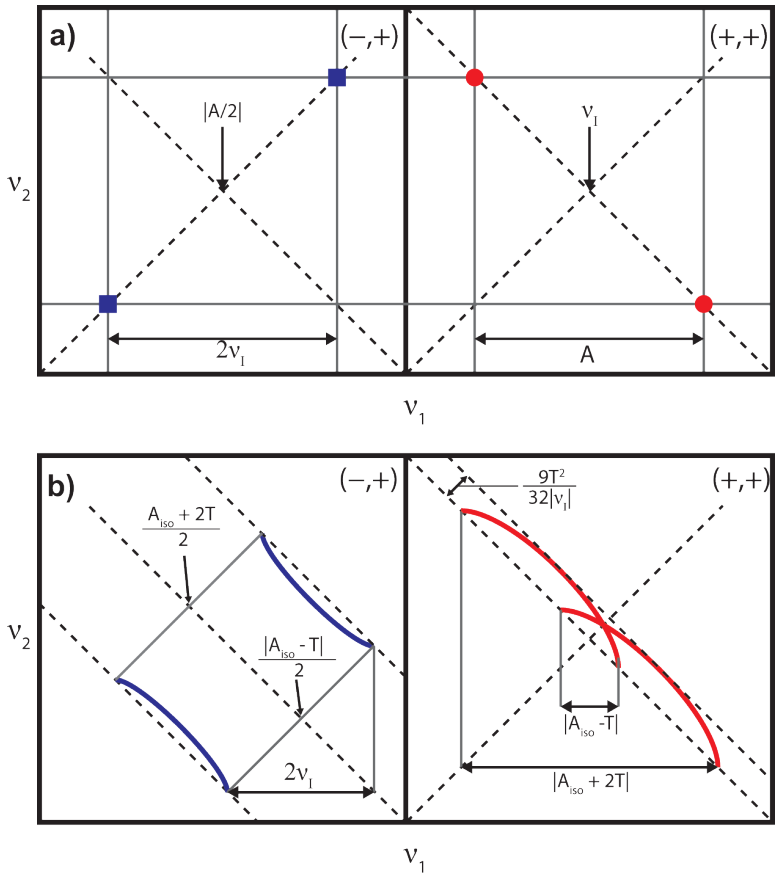

Figure S1. a) HYSCORE powder patterns for an $S = 1/2$, $I = 1/2$ spin system with an isotropic hyperfine tensor A. b) HYSCORE powder patterns for an $S = 1/2$, $I = 1/2$ spin system with an isotropic hyperfine tensor which contains isotropic (a_{iso}) and dipolar (T) contributions. Blue correlation ridges represent the strong coupling case; red correlation ridges represent the weak coupling case.

EPR Simulations. Simulations of all CW and pulse EPR data were achieved using the EasySpin[6] simulation toolbox (release 5.2.21) with Matlab 2018b using the following Hamiltonian:

$$\hat{H} = \mu_B \vec{B}_0 g \hat{S} + \mu_N g_N \vec{B}_0 \hat{I} + h\hat{S} \cdot \mathbf{A} \cdot \hat{I} + h\hat{I} \cdot \mathbf{P} \cdot \hat{I} \quad (3)$$

In this expression, the first term corresponds to the electron Zeeman interaction term where μ_B is the Bohr magneton, g is the electron spin g-value matrix with principle components g = [g_{xx} g_{yy} g_{zz}], and $\hat{S}$ is the electron spin operator; the second term corresponds to the nuclear Zeeman interaction term where μ_N is the nuclear magneton, g_N is the characteristic nuclear g-value for each nucleus (e.g. ^1H, ^2H, ^{31}P) and $\hat{I}$ is the nuclear spin operator; the third term corresponds to the electron-nuclear hyperfine term, where **A** is the hyperfine coupling tensor with principle components **A** = [A_{xx}, A_{yy}, A_{zz}]; and for nuclei with $I \geq 1$, the final term corresponds to the nuclear quadrupole (NQI) term which arises from the interaction of the nuclear quadrupole moment with the local electric field gradient (efg) at the nucleus, where **P** is the quadrupole coupling tensor. In the principle axis system (PAS), **P** is traceless and parametrized by the quadrupole coupling constant e^2Qq/h and the asymmetry parameter η such that:

$$\mathbf{P} = \begin{pmatrix} P_{xx} & 0 & 0 \\ 0 & P_{yy} & 0 \\ 0 & 0 & P_{zz} \end{pmatrix} = \frac{e^2Qq/h}{4I(2I-1)} \begin{pmatrix} -(1-\eta) & 0 & 0 \\ 0 & -(1+\eta) & 0 \\ 0 & 0 & 2 \end{pmatrix} \quad (4)$$

where $\frac{e^2Qq}{h} = 2I(2I-1)P_{zz}$ and $\eta = \frac{P_{xx}-P_{yy}}{P_{zz}}$. The asymmetry parameter may have values between 0 and 1, with 0 corresponding to an electric field gradient with axial symmetry and 1 corresponding to a fully rhombic efg.

The orientations between the hyperfine and NQI tensor principle axis systems and the g-matrix reference frame are defined by the Euler angles (α, β, γ), with rotations performed within the zyz convention where α rotates xyz counterclockwise about z-axis to give x'y'z', β rotates x'y'z counterclockwise about y'-axis to give x",y",z", γ rotates xyz counterclockwise about z"-axis to give final frame orientation.

VII. Electrochemistry:

Electrochemical measurements were carried out using a CD instruments 600B electrochemical analyzer. A freshly polished glassy carbon electrode was used as the working electrode and a graphite rod was used as the auxiliary electrode. Solutions (THF) of electrolyte (0.4 M tetra-n-butylammonium hexafluorophosphate) contained ferrocene (0.1 mM), to serve as an internal reference, and analyte (0.2 mM). All reported potentials are referenced to the ferrocene/ferrocenium couple, $[Cp_2Fe]^+$ /Cp_2Fe.

VIII. Synthetic Procedures:

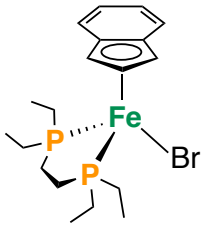

Fe(η^3:η^2-Ind)(depe)(Br) (1): To a solution of *trans*-$FeBr_2(depe)_2$ (402 mg, 0.64 mmol, 1 equiv.) in THF at -78 ˚C was added drop-wise a chilled (-78 ˚C) solution of lithium indenide (78 mg, 0.64 mmol, 1 equiv.). Following addition, the resulting mixture was stirred for an additional 2 h at room temperature, giving a clear purple solution. Subsequently, all volatiles were removed *in-vacuo* and the residue was washed with pentane (2 x 20 mL) and Et_2O (2 x 20 mL). The resulting purple solid was dissolved in THF and filtered through a pad of Celite®. Cooling a pentane-layered THF solution at –35 ºC afforded **1** as dark purple crystals (132 mg, 45%). ***N.B.*** Allowing this reaction mixture to stir for longer than 2 h results in appreciable formation of $Fe(Ind)_2$ and free ligand.

^{1}H NMR (C_6D_6, 400 MHz, 298 K): δ = 7.54 (m, 2H), 7.10 (m, 2H), 4.56 (br s, 1H), 4.01 (br s, 2H), 2.13 (m, 2H), 1.79 (m, 2H), 1.64 (m, 2H), 1.28 (m, 2H), 1.12 (m, 4H), 1.01 (m, 6H), 0.77 (m, 6H). **^{31}P{^{1}H} NMR (C_6D_6, 162 MHz, 298 K)**: δ = 92.98. **^{13}C NMR (THF-d_8, 100 MHz, 298 K)**: δ = 127.99, 125.39, 83.13 (η^3:η^2-C_9H_7), 58.07 (η^3:η^2-C_9H_7), 23.60, 21.92, 20.40, 10.13, 8.99. **CV data (1 mM, vs. Fc/Fc$^+$)**: - 0.53 V (Fe^{II}/Fe^{III}). **UV-VIS (THF, 1 cm cell, 298 K)**: λ = 529 {313 $M^{-1}cm^{-1}$}, 687 {208 $M^{-1}cm^{-1}$}. **Anal. Calcd.** for $C_{19}H_{31}BrFeP_2$ (456.04): C, 49.92; H, 6.84. Found: C, 50.40; H, 6.96.

Figure S2. 1, ^{1}H NMR, C_6D_6, 400 MHz, 298 K

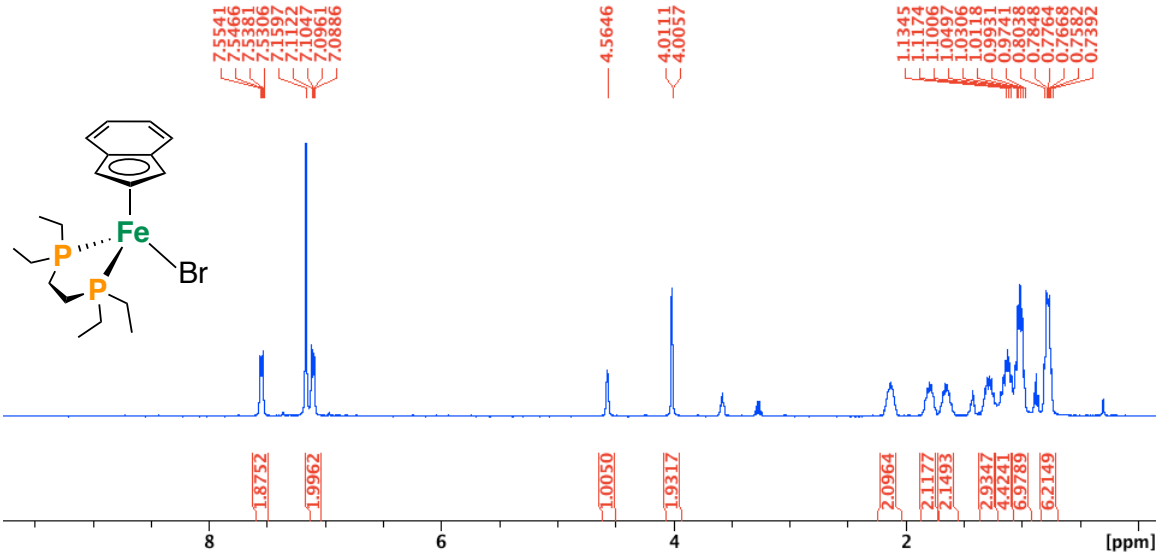

Figure S3. 1, $^{31}P\{^{1}H\}$ NMR, C_6D_6, 162 MHz, 298 K

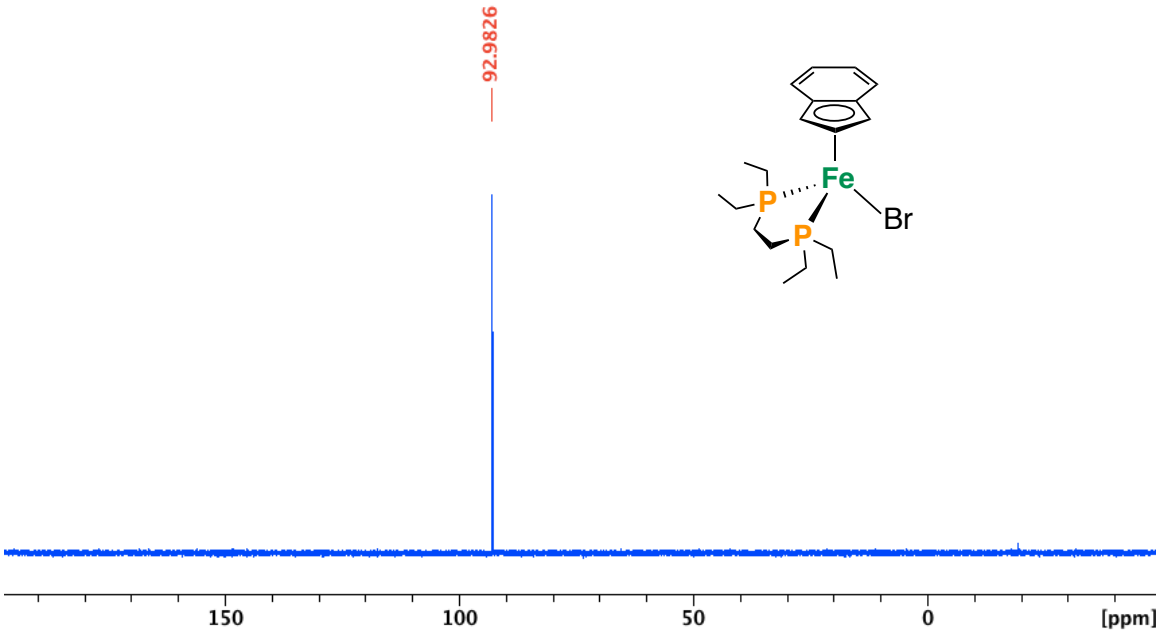

Figure S4. 1, $^{31}C\{^{1}H\}$ NMR, THF-d_8, 100 MHz, 298 K

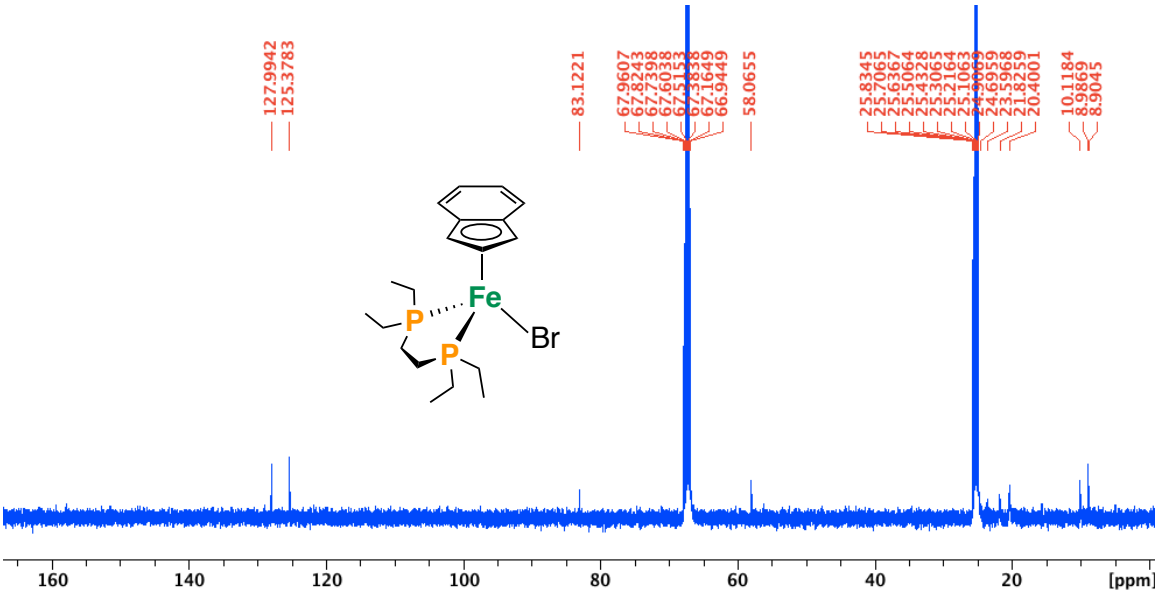

Figure S5. 1, UV-Visible spectrum, THF, 298 K (λ = 529, 687 nm)

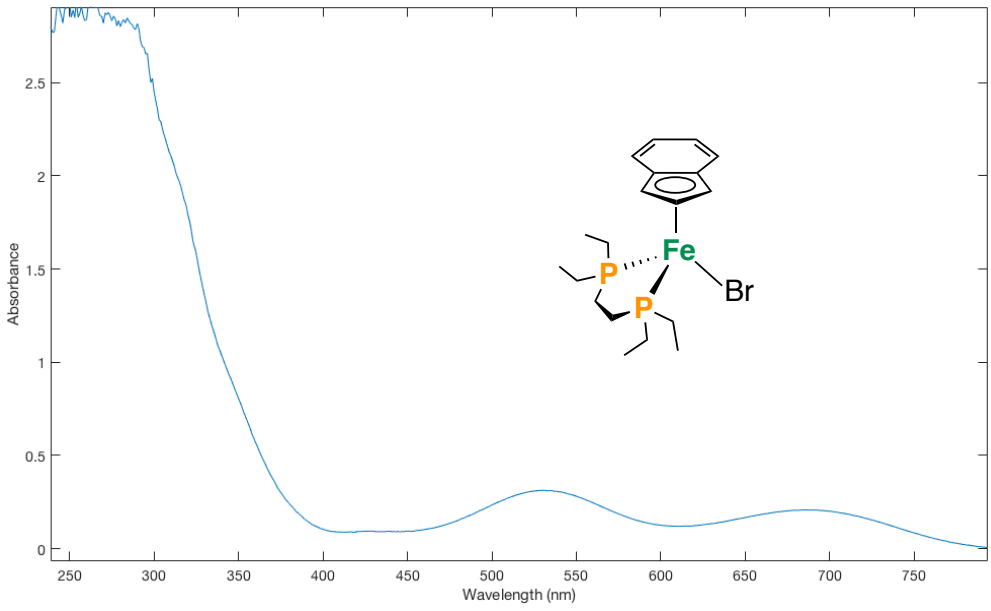

Fe(η^3:η^2-Ind)(depe)(H) (**2**): To a solution of **1** (21.5 mg, 0.047 mmol, 1 equiv.) in THF at -78 ˚C was added drop-wise a chilled (-78 ˚C) 1.0 M solution of Li[BEt_3H] (47.1 µL, 0.047 mmol, 1 equiv.). Following addition, the resulting mixture was stirred for an additional 10 min at -78 ˚C and then at room temperature for 2 h, giving a clear red solution. Subsequently, all volatiles were removed *in-vacuo* and the residue was dissolved in pentane (5 mL) and filtered through a pad of Celite®. This was repeated three times to give **2** as a red oil (17.5 mg, 98%). Efforts to recrystallize **2** were unsuccessful.

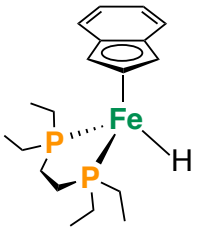

^{1}H NMR (C_6D_6, 400 MHz, 298 K): δ = 7.39 (m, 2H), 6.81 (m, 2H), 4.73 (br s, 2H), 4.71 (m, 1H), 1.57-1.34 (m, 8H), 1.25 (m, 4H), 0.99 (m, 6H), 0.75 (m, 6H), -20.64 (t, $^2J_{H,P}$ = 70.8 Hz, $^1J_{Fe,H}$ = 10.3 Hz). **^{31}P{^{1}H} NMR (C_6D_6, 162 MHz, 298 K)**: δ = 106.38 ($^2J_{H,P}$ = 70.8 Hz, $^1J_{Fe,P}$ = 60.3 Hz). **^{13}C NMR (C_6D_6, 100 MHz, 298 K)**: δ = 126.69, 121.00, 97.73, 80.09 (η^3:η^2-C_9H_7), 62.22 (η^3:η^2-C_9H_7), 27.01 (m), 25.89 (dd, $J_{C,P}$ = 21.4 Hz, $J_{C,P}$ = 19.5 Hz), 25.24 (dd, $J_{C,P}$ = 6.9 Hz, $J_{C,P}$ = 4.89 Hz), 9.27, 9.14. **IR (thin film, 298 K, cm^{-1})**: 1851 cm^{-1} (υ_{FeH}). **^{57}Fe Mössbauer (80 K, Et_2O solution, mm/s)**: δ = 0.28, ΔE_Q = 1.61. **CV data (1 mM, vs. Fc/Fc$^+$)**: - 0.81 V (Fe^{II}/Fe^{III}). **UV-VIS (THF, 1 cm cell, 298 K)**: λ = 396 {498 M^{-1}cm^{-1}}, 506 {912 M^{-1}cm^{-1}}. *N.B*. Given the physical nature of **2**, elemental analysis was not acquired.

Probing bimolecular H_2 loss:

To a *J. Young* NMR tube cooled to -78 ºC containing a THF-d_8 solution (300 µL) of 4.5 mg (12 µmol) **2-H** and 4.5 mg (12 µmol) **2-D** (500 µL) was added 25.6 mg (25 µmol) [Fc]BAr^F_4 in 200 µL THF-d_8. The tube was shaken and warmed to room temperature. NMR spectroscopy confirms the presence of both H_2 and HD. **^{1}H NMR (THF-d_8, 400 MHz, 298 K)**: δ = 4.50 ppm (t, $^1J_{H,D}$ = 42 Hz; HD), 4.55 (s, H_2).

Figure S6. 2, ^{1}H NMR, C_6D_6, 400 MHz, 298 K

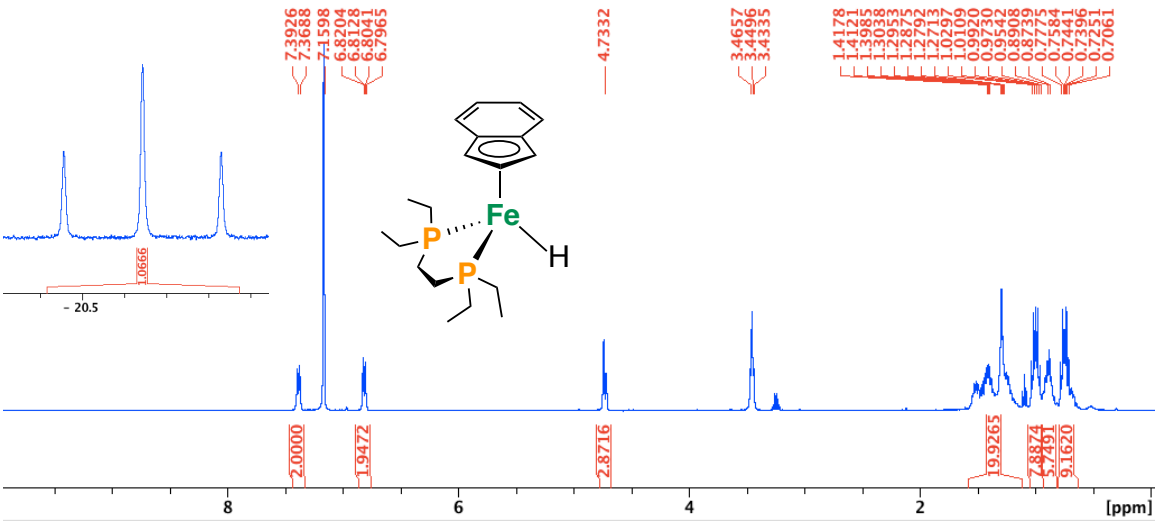

Figure S7. 2, $^{31}P\{^{1}H\}$ NMR, C_6D_6, 162 MHz, 298 K

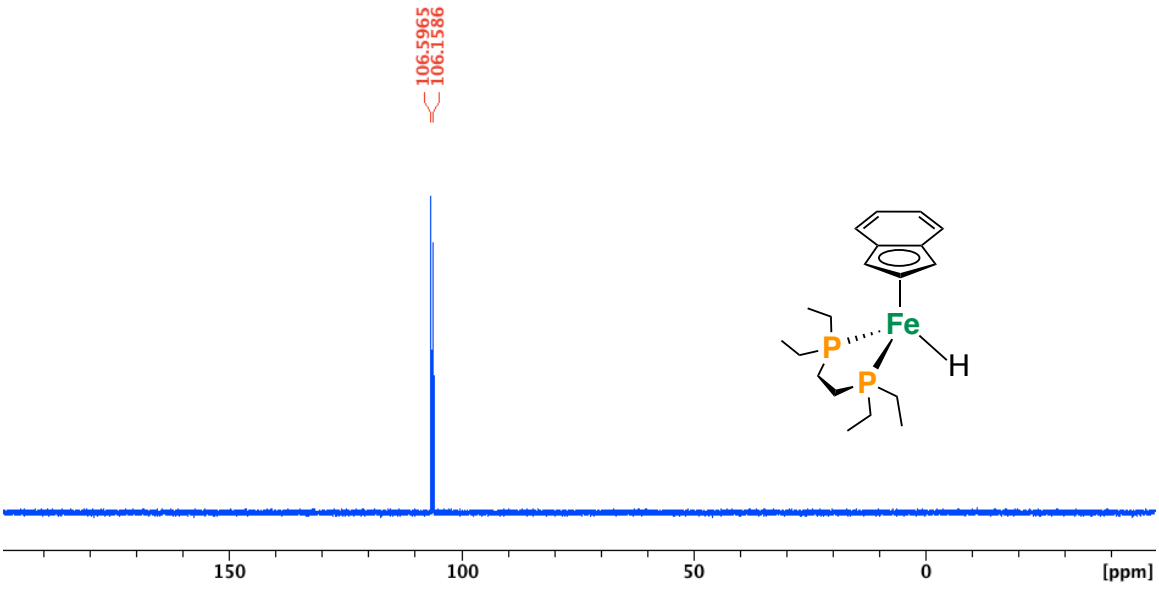

Figure S8. 2-^{57}Fe, ^{1}H NMR, C_6D_6, 400 MHz, 298 K

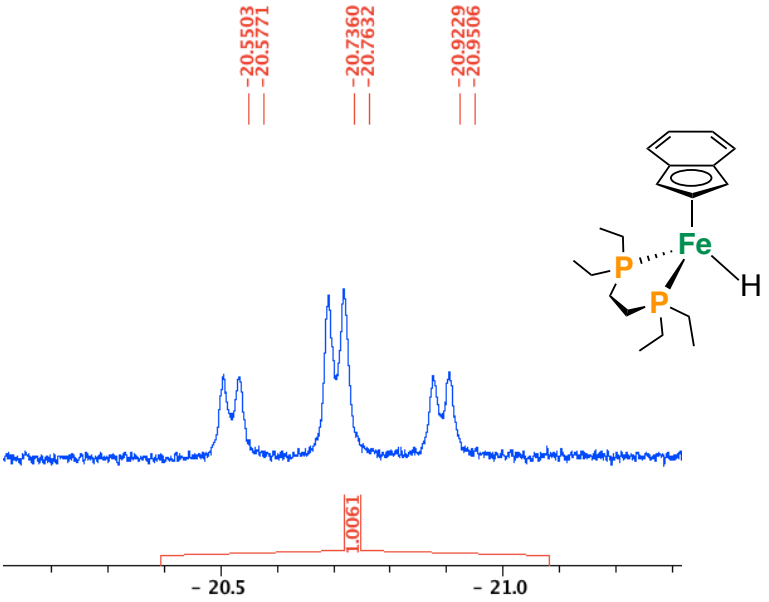

Figure S9. 2-^{57}Fe, ^{31}P{^{1}H} NMR, C_6D_6, 162 MHz, 298 K

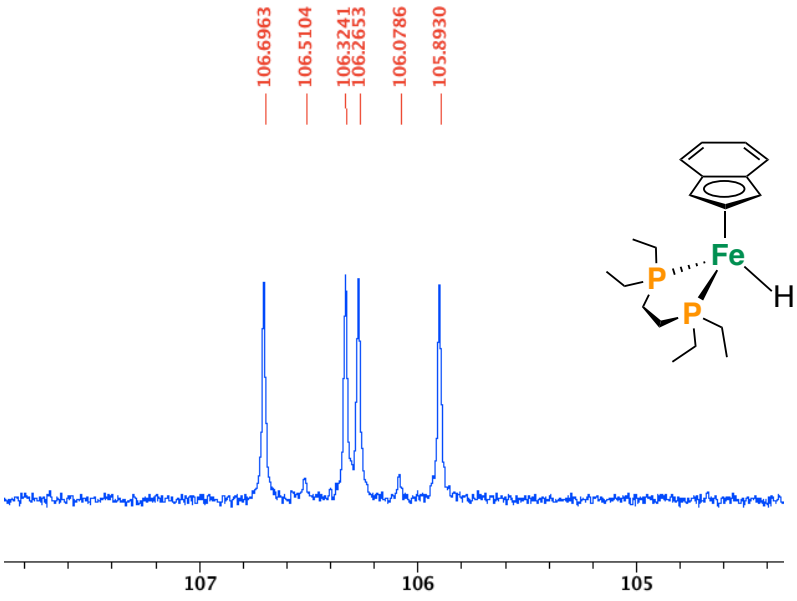

Figure S10. 2, $^{31}C\{^{1}H\}$ NMR, C_6D_6, 100 MHz, 298 K

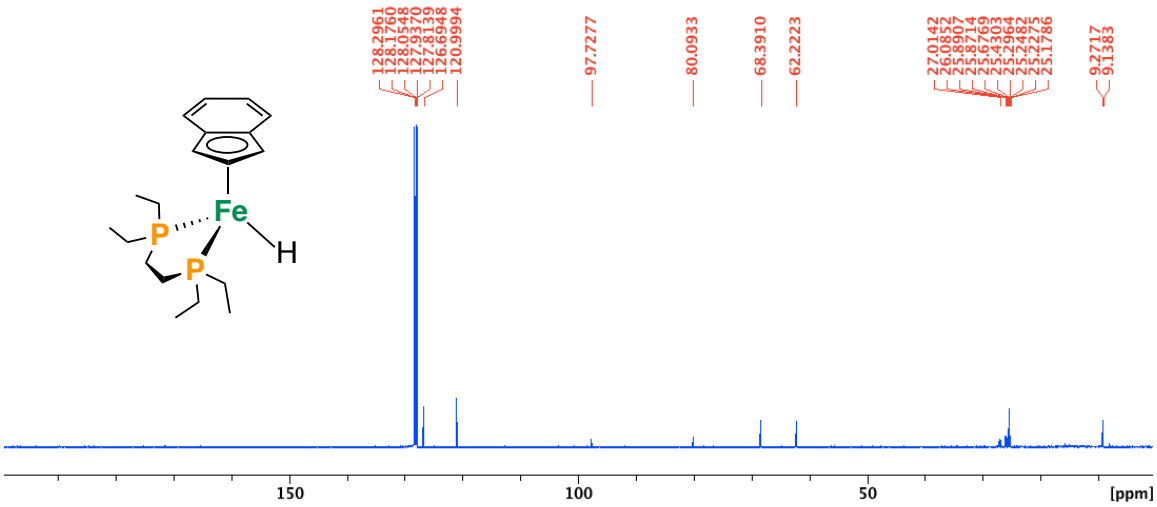

Figure S11. 2, FT-IR ATR, thin film, 298 K (υ_{FeH} = 1851 cm^{-1})

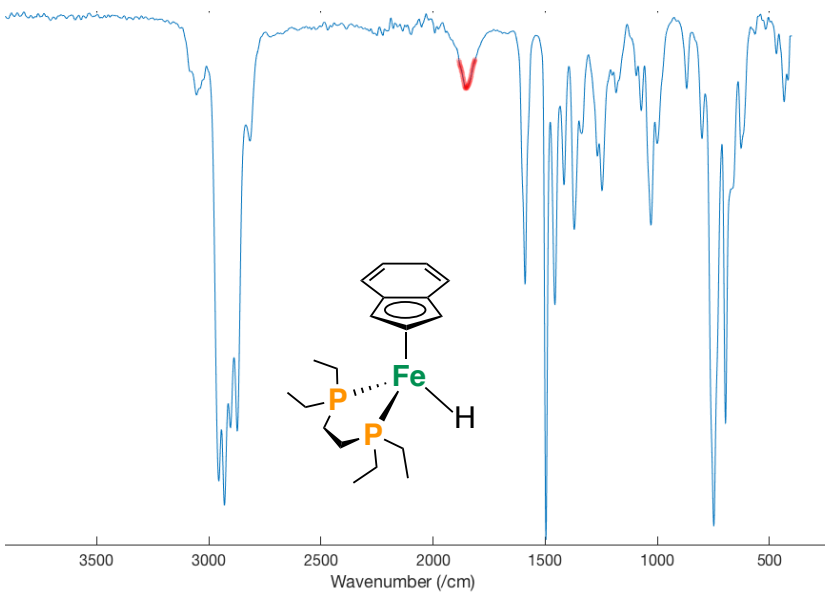

Figure S12. 2, 80 K ^{57}Fe Mössbauer spectrum collected in the presence of a 50 mT magnetic field oriented parallel to the propagation of the γ-beam (frozen solution in Et_2O). $\delta = 0.28$ mm/s, $\Delta E_Q = 1.61$ mm/s. $\Gamma_L = \Gamma_R = +0.50$ mm/s.

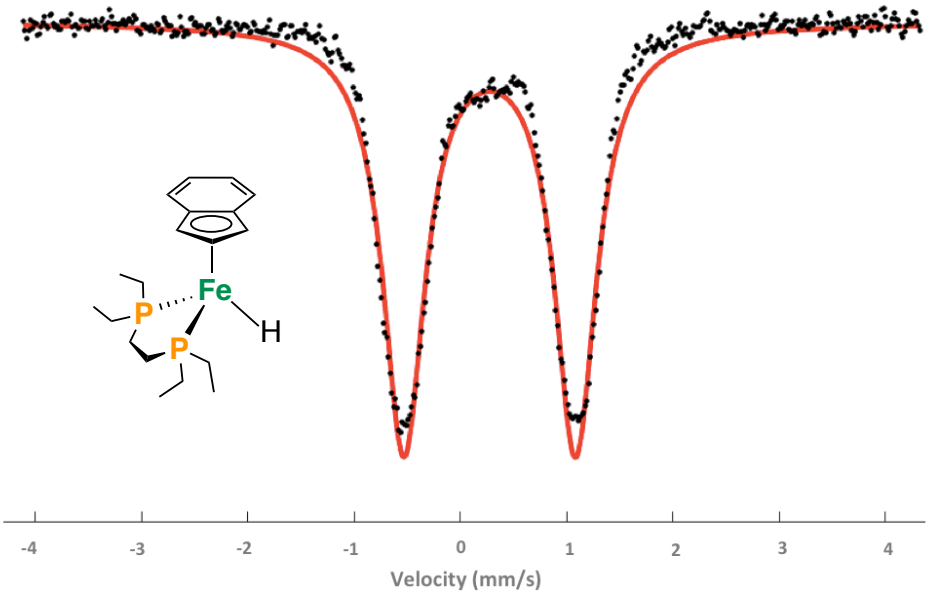

Figure S13. 2, Cylic Voltammogram, THF, 298 K showing a reversible feature at - 0.81 V for the Fe(II)/Fe(III) couple (vs. Fc/Fc$^+$) in 4 mL THF, 0.4 M $[NBu_4][PF_6]$ and analyte (1 mM). Data was collected at x mV/s with Pt counter, glassy carbon working, and Ag/AgOTf reference electrodes (■ 100 mV/s, ■ 200 mV/s, ■ 300 mV/s, and ■ 400 mV/s).

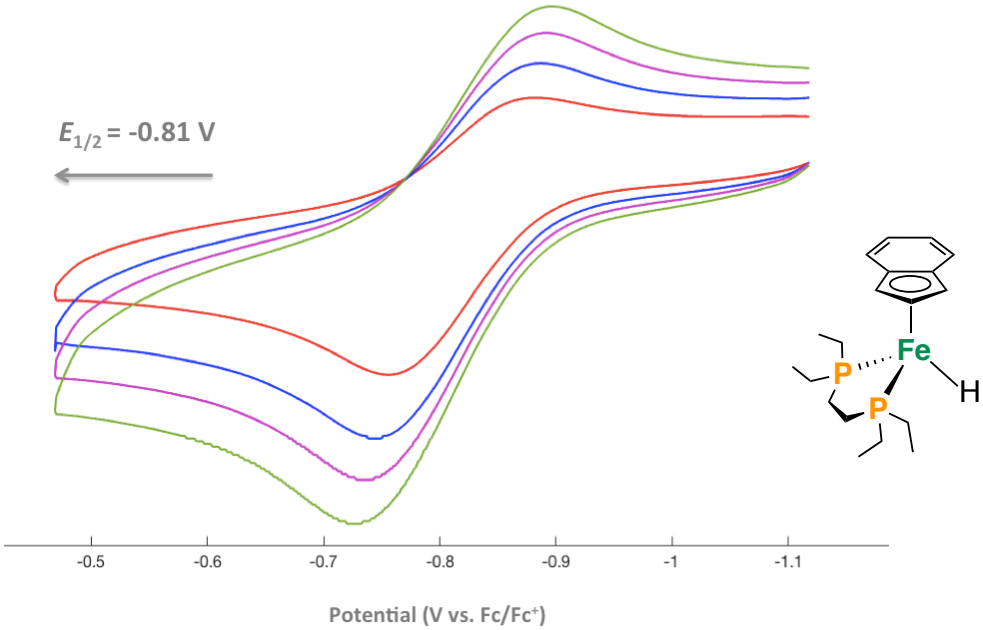

Figure S14. 2, UV-Visible spectrum, THF, 298 K (λ = 396, 506 nm)

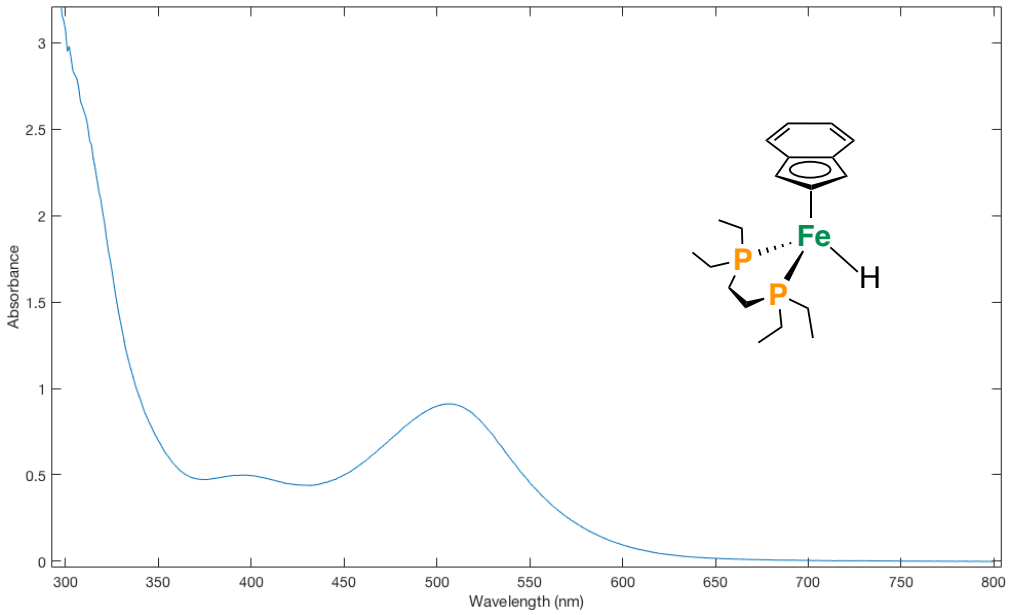

[Fe(η^6-IndH)(depe)][BAr^F_4] [**4**][BAr^F_4]: To a solution of **2** (12.9 mg, 0.034 mmol, 1 equiv.) in Et_2O at -78 ˚C was added drop-wise a chilled (-78 ˚C) solution of Fc[BAr^F_4] (35.9 mg, 0.034 mmol, 1 equiv.). Following addition, the resulting dark orange mixture was stirred for an additional 20 min at -78 ˚C and then all volatiles were removed *in-vacuo* at -78 ˚C. Next, the residue was washed with 20 mL cold (-78 ˚C) pentane, dissolved in cold (-78 ˚C) Et_2O, layered with pentane and placed in the freezer at -35 ˚C causing deposition of yellow ([**4**][BAr^F_4]) and purple ([**7**][BAr^F_4]$_2$) crystals. *N.B*. Considerably fewer (~ 1:10) orange crystals were observed.

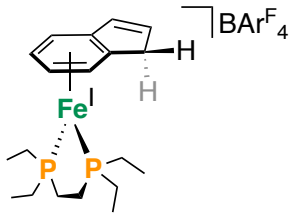

Yield: According to a ^{57}Fe Mössbauer experiment, oxidation of **2**-^{57}Fe at -78 ºC produces *ca*. 30% of [**4**]$^+$ after 5 min.

^{57}Fe Mössbauer (80 K, Et_2O solution, mm/s): δ = 0.59 mm/s, ΔE_Q = 1.80 mm/s. **X-Band EPR (77 K, 2-MeTHF):** Sys.g = [2.332, 2.042, 1.992], Sys.lw = 1.2, Sys.Nucs = '^{31}P, ^{31}P', Sys.A = [86, 104, 100; 93, 88, 94], Sys.HStrain = [319 67 11], Exp.mwFreq = 9.389.

Figure S15. [**4**][BAr^F_4], 77 K X-band EPR spectrum in 2-MeTHF with simulations; blue trace: experiment; red trace: simulation (Sys.g = [2.332, 2.042, 1.992], Sys.lw = 1.2, Sys.Nucs = '^{31}P, ^{31}P', Sys.A = [86, 104, 100; 93, 88, 94], Sys.HStrain = [319 67 11], Exp.mwFreq = 9.389].

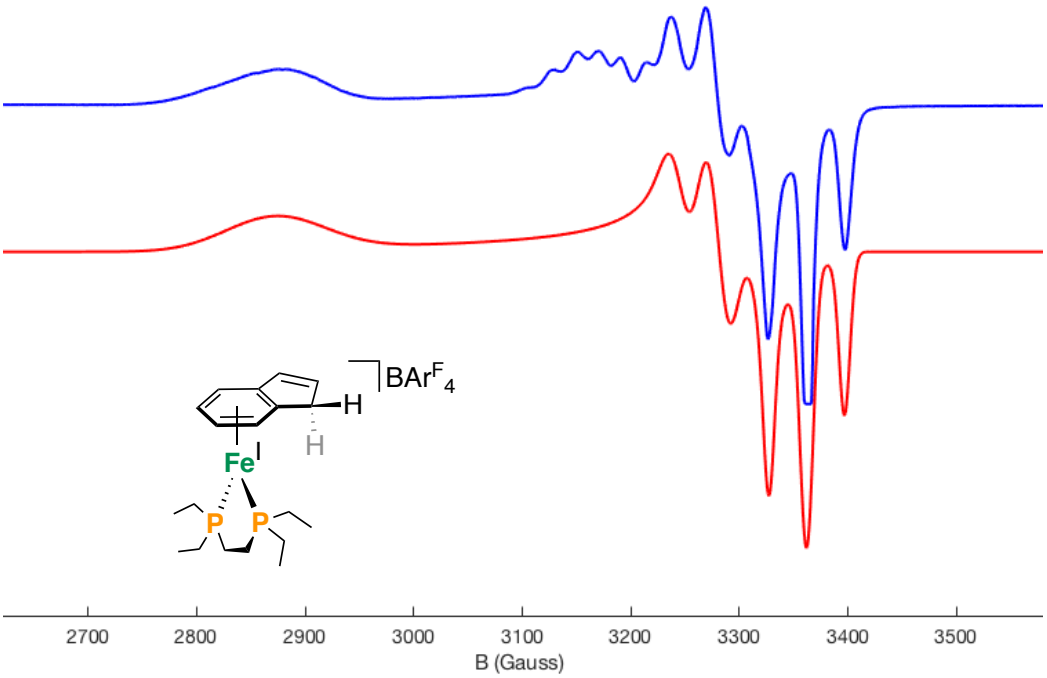

Figure S16. 80 K ^{57}Fe Mössbauer spectrum collected in the presence of a 50 mT magnetic field oriented parallel to the propagation of the γ-beam (frozen solution in 2-MeTHF).

Addition of [Fc]BAr^F_4 to **2-^{57}Fe** at -78 °C. Top spectrum shows freeze-quenched sample after 5 min. Bottom spectrum shows freeze-quench after stirring at room temperature for 15 min. Parameters: δ = 0.23 mm/s, ΔE_Q = 1.73 mm/s (**green, 42%**); δ = 0.59 mm/s, ΔE_Q = 1.80 mm/s (**blue, 28%**), δ = 0.40 mm/s, ΔE_Q = 0.46 mm/s (**violet, 16%**); $\Gamma_L = \Gamma_R$ = - 0.50 mm/s. *N.B.* These fits are not strictly required by the data.

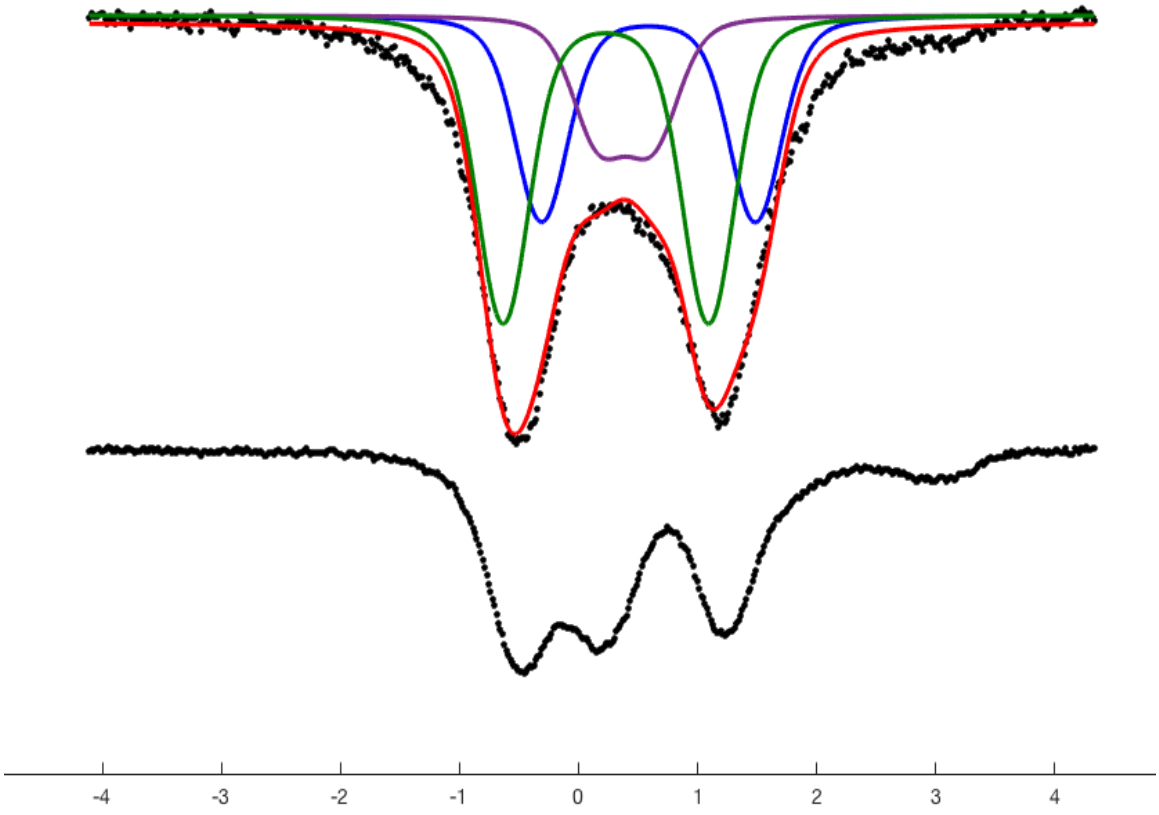

[Fe(η^6-toluene)(dippe)][BAr$^F_4$] [**5**][BAr$^F_4$]: To a solution of Fe^0(η^6-toluene)(dippe) (16.7 mg, 0.041 mmol, 1 equiv.) in Et_2O at -78 ˚C was added drop-wise a chilled (-78 ˚C) solution of Fc[BAr$^F_4$] (38.4 mg, 0.037 mmol, 0.9 equiv.). Following addition, the resulting dark orange mixture was stirred for an additional 10 min at -78 ˚C and then at room temperature for 10 min. Next, all volatiles were removed *in-vacuo* and the orange residue was washed with 20 mL pentane. Cooling a pentane-layered THF solution at –35 ºC afforded [**7**][BAr$^F_4$] as orange crystals (40 mg, 77%).

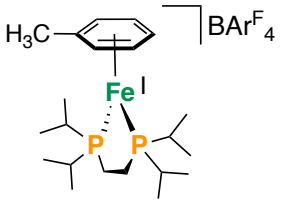

^{1}H NMR (THF-d$_8$, 400 MHz, 298 K): δ = 35.37, 19.83, 7.78 (BAr$^F_4$), 7.56 (BAr$^F_4$), 6.60, 3.04, -0.17, -7.04. **X-Band EPR (77 K, 2-MeTHF)**: Sys.g = [2.371, 2.032, 1.990], Sys.lw = 1.2, Sys.Nucs = '^{31}P, ^{31}P', Sys.A = [--, 90, 105; --, 99, 89], Sys.HStrain = [256 71 10], Exp.mwFreq = 9.389 mT. **^{57}Fe Mössbauer (160 K, frozen THF solution, mm/s)**: δ = 0.50 ΔE_Q = 1.71. **CV data (1 mM, vs. Fc/Fc$^+$)**: - 1.51 V (Fe^I/Fe^0). **UV-VIS (THF, 1 cm cell, 298 K)**: λ = 267 {3231 M^{-1}cm^{-1}}, 280 {2615 M^{-1}cm^{-1}}, 352 {849 M^{-1}cm^{-1}}, 428 {282 M^{-1}cm^{-1}}. **Anal. Calcd.** for $C_{53}H_{52}BF_{24}FeP_2$ (1273.3): C, 49.98; H, 4.12. Found: C, 51.20; H, 4.66.

Figure S17. [**5**][BAr^F_4], ^1H NMR, THF-d_8, 400 MHz, 298 K

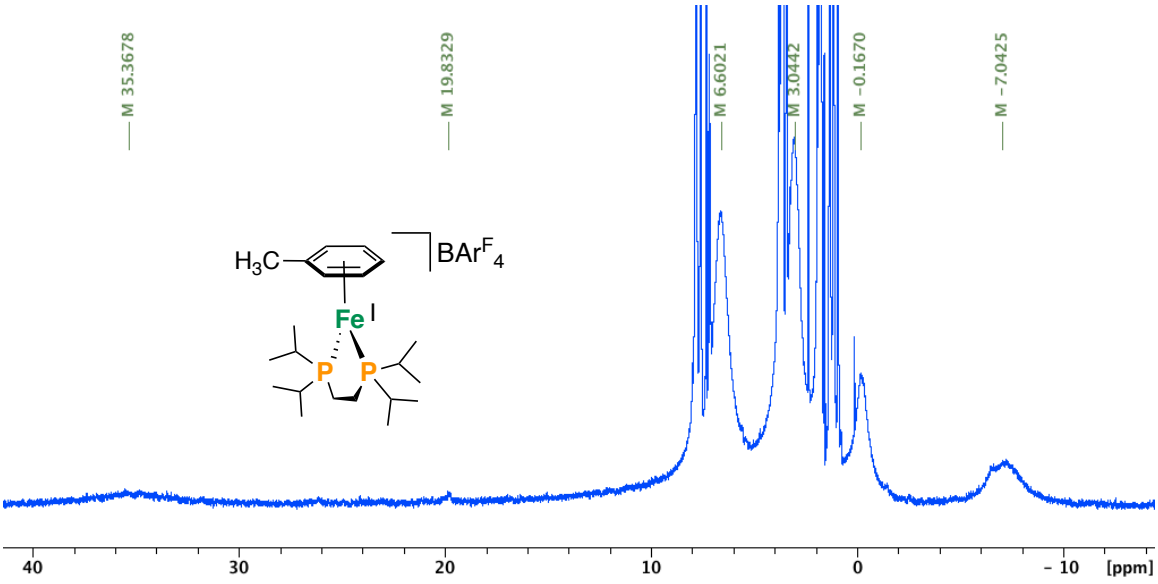

Figure S18. [**5**][BAr^F_4], ^1H NMR (expanded view), THF-d_8, 400 MHz, 298 K

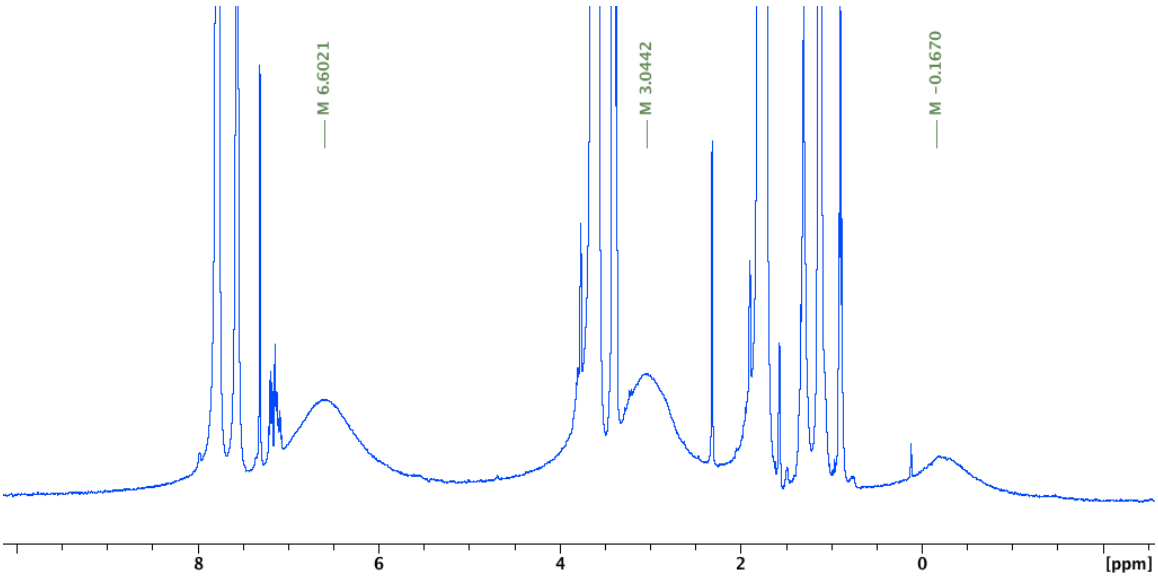

Figure S19. [**5**][BAr^F_4], 77 K X-band EPR spectrum in 2-MeTHF with simulations; blue trace: experiment; red trace: simulation. Sys.g = [2.371, 2.032, 1.990], Sys.lw = 1.2, Sys.Nucs = '^{31}P, ^{31}P', Sys.A = [--, 90, 105; --, 99, 89], Sys.HStrain = [256 81 40], Exp.mwFreq = 9.389].

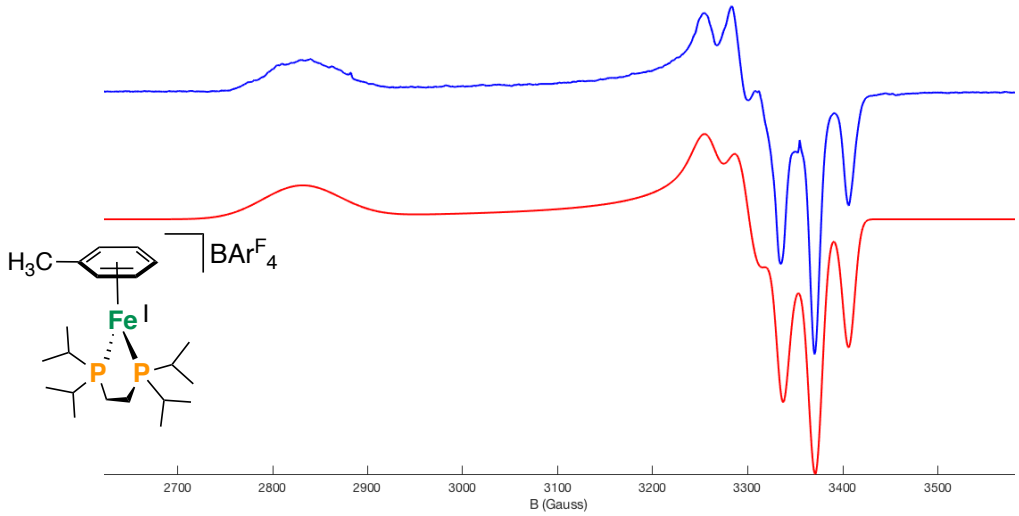

Figure S20. [**5**][BAr^F_4], 80 K (bottom) and 160 K (top) ^{57}Fe Mössbauer spectrum collected in the presence of a 50 mT magnetic field oriented parallel to the propagation of the γ-beam (frozen solution in Et_2O).): $\delta \sim 0.50$ mm/s, $\Delta E_Q \sim 1.71$ mm/s.

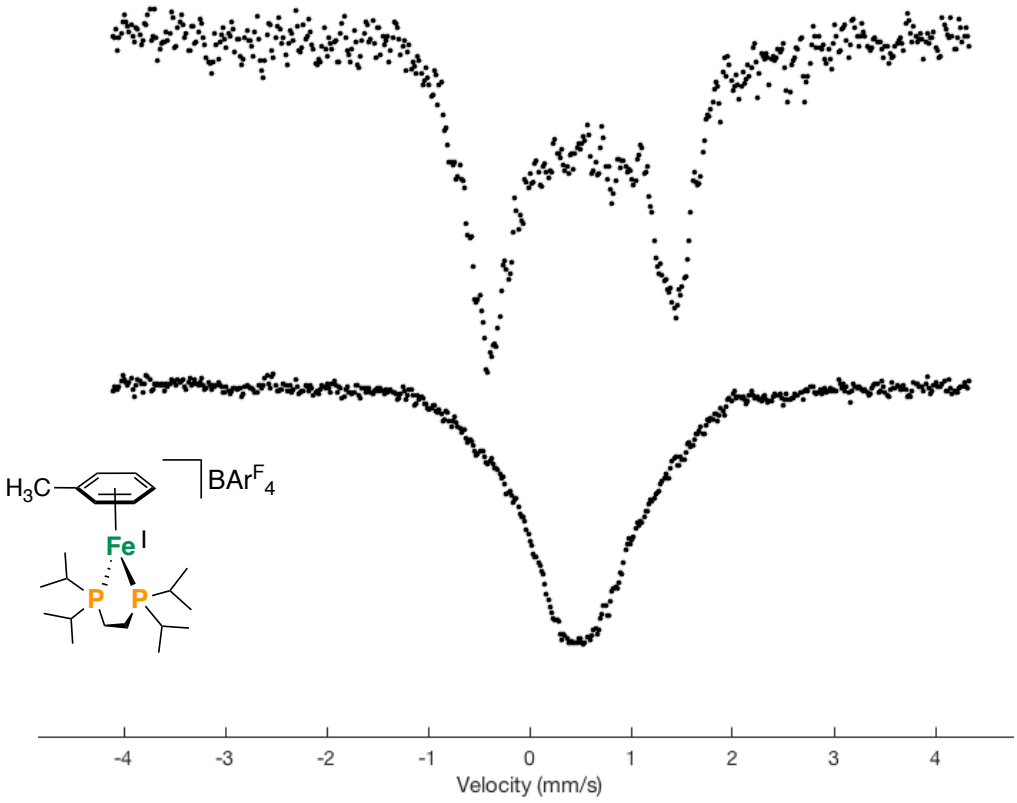

Figure S21. [**5**][BAr^F_4], Cylic Voltammogram, THF, 298 K showing a reversible feature at -1.51 V for the Fe(I)/Fe(0) couple (vs. Fc/Fc^+) in 4 mL THF, 0.4 M [NBu_4][PF_6] and analyte (1 mM). Data was collected at 100 mV/s with Pt counter, glassy carbon working, and Ag/AgOTf reference electrodes

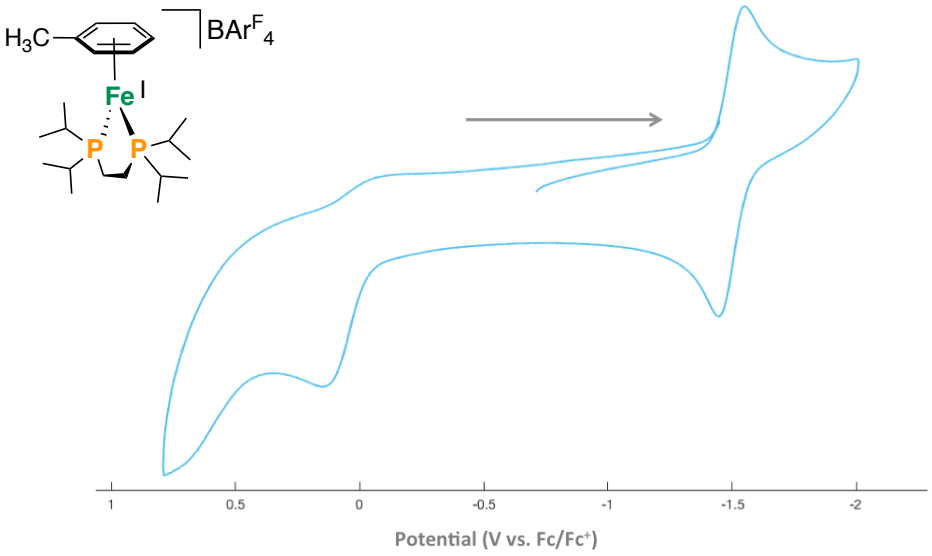

Figure S22. [**5**][BAr^F_4], Cylic Voltammogram, THF, 298 K showing a reversible feature at -1.51 V for the Fe(I)/Fe(0) couple (vs. Fc/Fc^+) as a function of scan rate (■ 50 mV/s to ■ 500 mV/s at 50 mV/s increments).

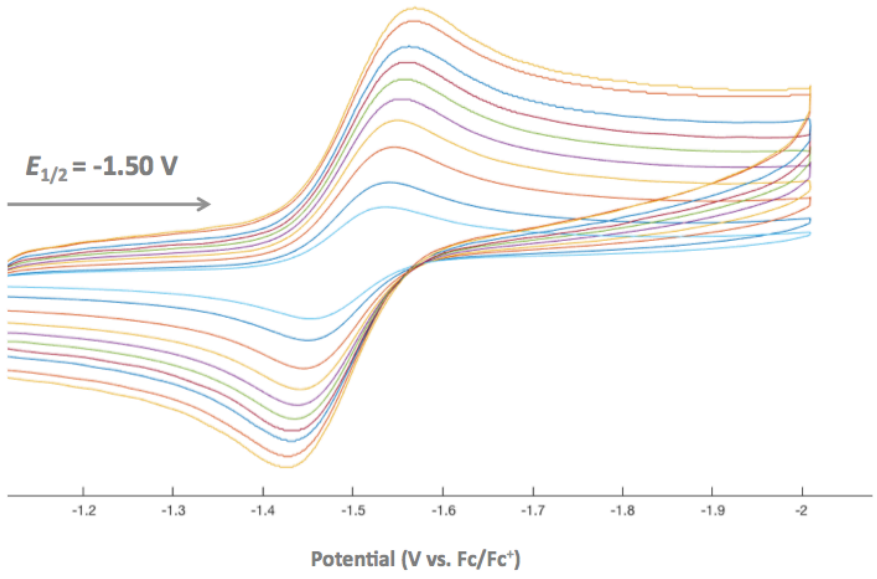

Figure S23. [**5**][BAr^F_4], UV-Visible spectrum, THF, 298 K (λ = 267, 280, 352, 428 nm)

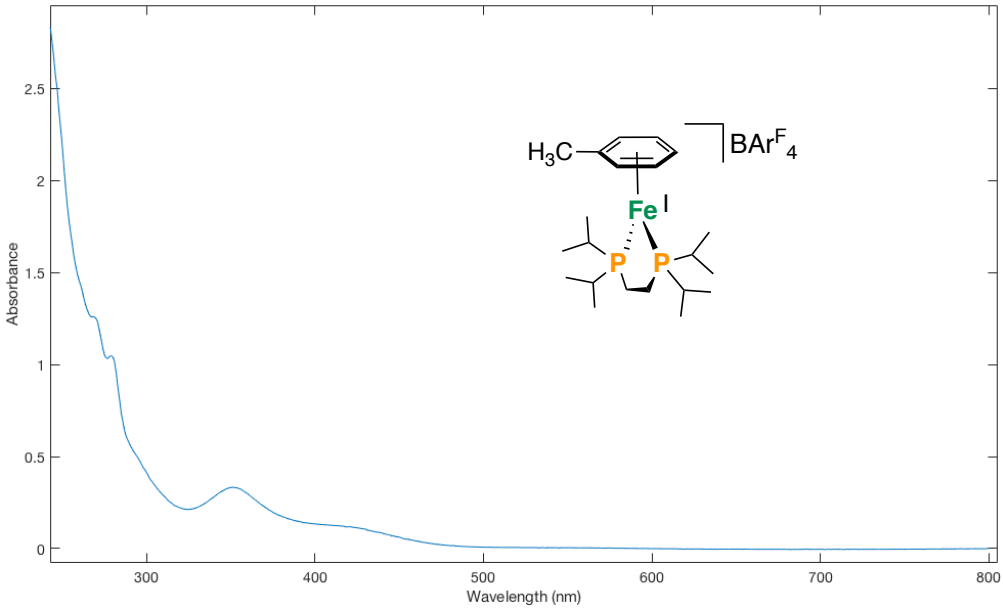

[Fe(η^3:η^2-Ind)(depe)N_2][BAr^F_4]$_2$ [**6**][BAr^F_4]: *N.B.* This compound can be prepared via treatment of **2** with Fc[BAr^F_4] or $H(OEt_2)_2$[BAr^F_4]. To a solution of **2** (22.1 mg, 0.058 mmol, 1 equiv.) in Et_2O (2 mL) at -78 ˚C was added drop-wise a chilled (-78 ˚C) solution of $H(OEt_2)_2$[BAr^F_4] (53.4 mg, 0.053 mmol, 0.9 equiv.) in Et_2O (2 mL). Following addition, the resulting mixture was stirred at -78 ˚C and warmed to 25 ˚C over 2 h. During this time, a purple solid ([**7**][BAr^F_4]$_2$) precipitated and was removed by filtration. The supernatant was dried *in-vacuo* and washed with pentane. Cooling a pentane-layered THF solution at –35 ºC afforded [**6**][BAr^F_4] as orange crystals that were mechanically separated from [**7**][BAr^F_4]$_2$ for analysis by X-ray diffraction. Complex [**6**][BAr^F_4] was not obtained in pure form, however, by $^{31}P\{^1H\}$ NMR spectroscopy, the yield is estimated to be ~30%. The N_2 ligand in [**6**][BAr^F_4] was also observed to be labile; exposure to vacuum caused a change in color from orange to maroon.

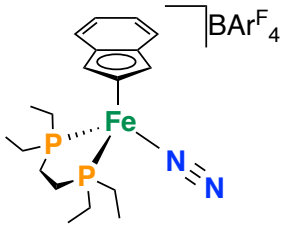

^{1}H NMR (THF-d_8, 400 MHz, 298 K, select signals): δ = 7.79 (s, 8H; BAr^F_4), 7.70 (m, 2H), 7.58 (br s, 4H, BAr^F_4), 7.47 (m, 2H), 5.23 (s, 1H), 5.01 (s, 2H). **$^{31}P\{^1H\}$ NMR (THF-d_8, 162 MHz, 298 K)**: δ = 89.7. **IR (thin film, 298 K, cm^{-1})**: 2151 cm^{-1} (υ_{NN}).

Figure S24. [**6**][BAr^F_4], $^{31}P\{^1H\}$ NMR, THF-d_8, 162 MHz, 298 K [signals at δ = 87.51 and 41.16 are due to [**7**][BAr^F_4]$_2$, those at δ = 56.0, 81.1, 87.3, and 92.9 ppm are due to impurities].

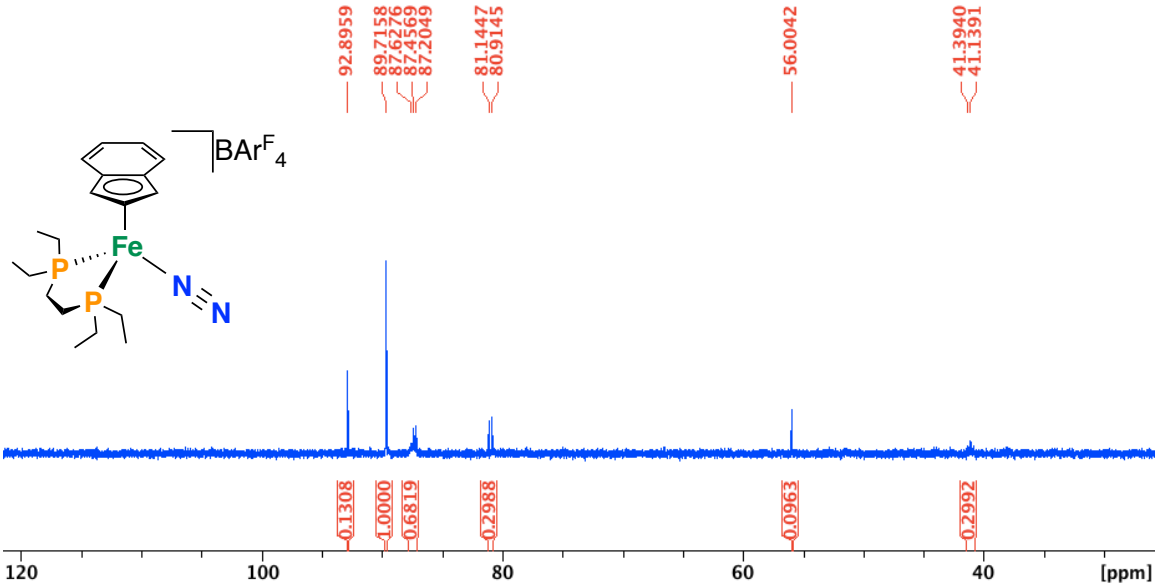

Figure S25. [**6**][BAr^F_4], FT-IR ATR, thin film, 298 K (υ_{NN} = 2151 cm^{-1})

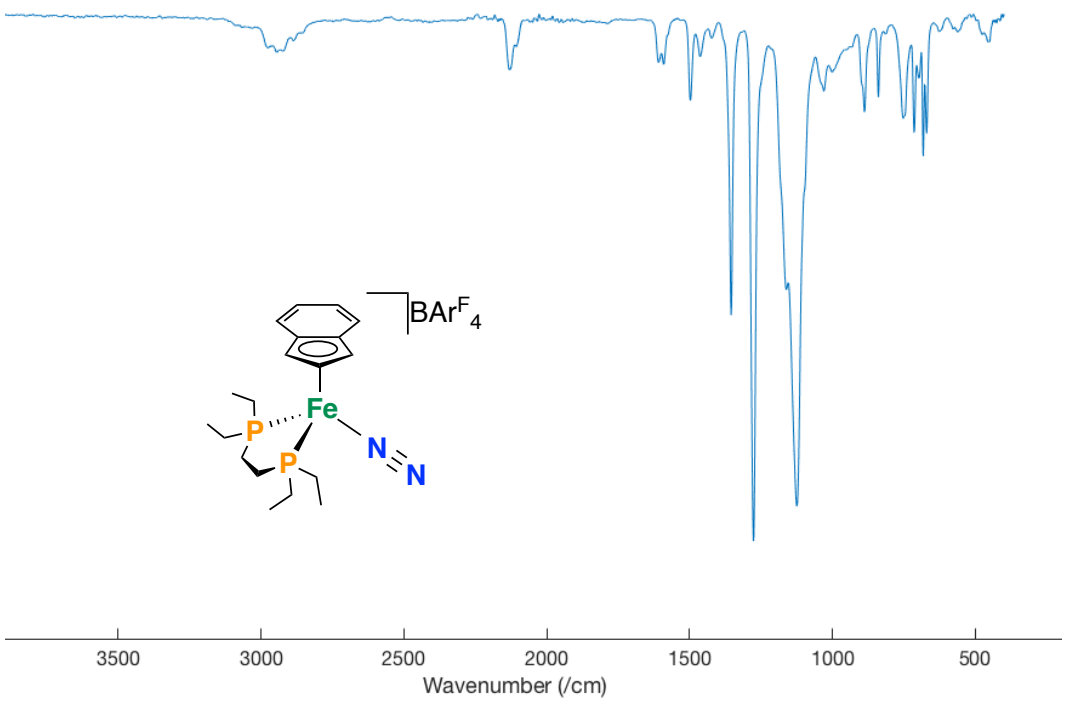

[Fe$_2$(η^3:η^2-Ind)$_2$(depe)$_2$(μ-depe)][BAr$^F_4$]$_2$ [**7**][BAr$^F_4$]$_2$: *N.B.* This compound can be prepared *via* treatment of **2** with Fc[BAr$^F_4$] or H(OEt)$_2$[BAr$^F_4$]. To a solution of **2** (22.1 mg, 0.058 mmol, 1 equiv.) in Et$_2$O (2 mL) at -78 ˚C was added drop-wise a chilled (-78 ˚C) solution of H(OEt$_2$)$_2$[BAr$^F_4$] (53.4 mg, 0.053 mmol, 0.9 equiv.) in Et$_2$O (2 mL). Following addition, the resulting mixture was stirred at -78 ˚C and warmed to 25 ˚C over 2 h. During this time, a purple solid precipitated that was isolated *via* filtration, washed with pentane, and dried *in-vacuo*. Cooling a pentane-layered THF solution at –35 ºC afforded [**7**][BAr$^F_4$]$_2$ as a dark purple crystals (11.4 mg, 22%).

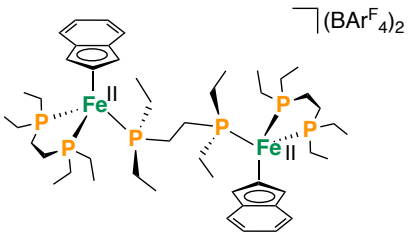

^{1}H NMR (THF-d$_8$, 400 MHz, 298 K): δ = 7.79 (s, 16H; BAr$^F_4$), 7.76 (m, 4H), 7.58 (br s, 8H, BAr$^F_4$), 7.41 (m, 2H), 5.39 (2H), 4.83 (m, 4H), 2.58 (m, 4H), 2.28-2.04 (m, 8H), 1.97 (m, 4H), 1.67 (m, 8H), 1.43 (m, 4H), 1.37-1.07 (m, 26H), 1.01 (m, 18H). **^{31}P{^{1}H} NMR (THF-d$_8$, 162 MHz, 298 K)**: δ = 87.51 (d, $^2J_{P,P}$ = 37.8 Hz), 41.16 (t, $^2J_{P,P}$ = 37.8 Hz). **^{13}C NMR (THF-d$_8$, 100 MHz, 298 K)**: δ = 162.63 (q, $^1J_{C,B}$ = 37 Hz, BAr$^F_4$, ipso quaternary C), 135.41 (BAr$^F_4$, ortho C), 129.81 (q, $^2J_{C,F}$ = 31 Hz, BAr$^F_4$, meta quaternary C), 128.76, 127.38, 124.93 (q, $^1J_{C,F}$ = 273 Hz, BAr$^F_4$, CF$_3$), 117.97 (m, BAr$^F_4$, para C), 104.28, 86.62 (η^3:η^2-C$_9$H$_7$), 64.62 (η^3:η^2-C$_9$H$_7$), 23.67 (br), 21.41 (br), 21.18 (br), 9.78 (br), 9.17 (br), 7.85 (br). **UV-VIS (THF, 1 cm cell, 298 K)**: λ = 329 {1657 M^{-1}cm^{-1}}, 491 {637 M^{-1}cm^{-1}}. **Anal. Calcd.** for C$_{112}$H$_{110}$B$_2$F$_{48}$Fe$_2$P$_6$ (2685.5): C, 50.06; H, 4.13. Found: C, 49.86; H, 4.21.

Figure S26. [**7**][BAr^F_4]$_2$, ^{1}H NMR, THF-d_8, 162 MHz, 298 K

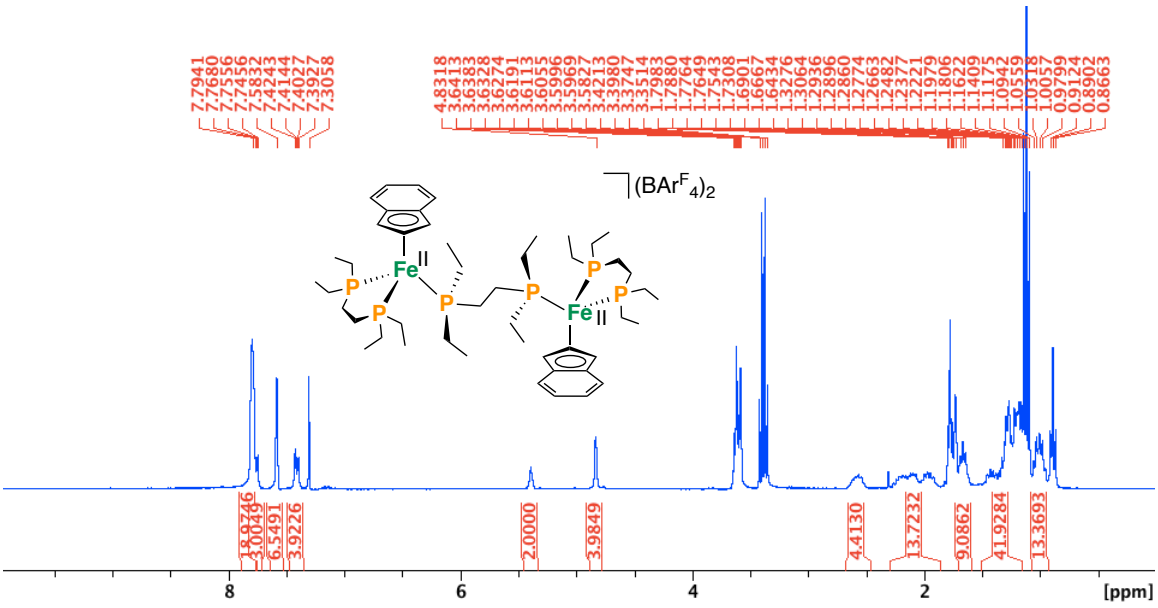

Figure S27. [**7**][BAr^F_4]$_2$, ^{31}P{^{1}H} NMR, THF-d_8, 162 MHz, 298 K

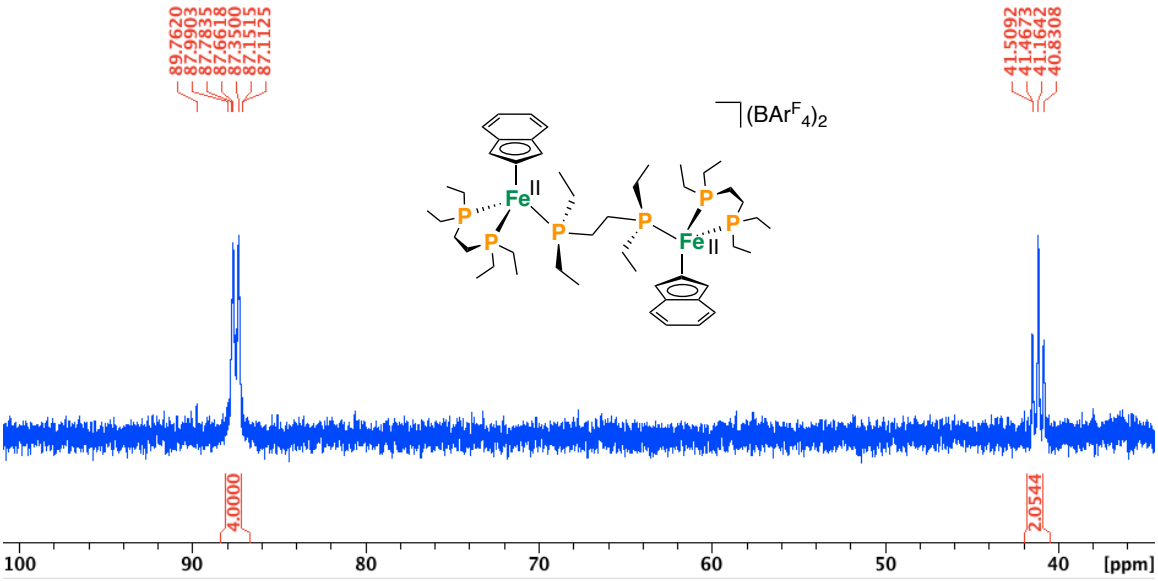

Figure S28. [**7**][BAr^F_4]$_2$, $^{31}C\{^1H\}$ NMR, THF-d_8, 100 MHz, 298 K

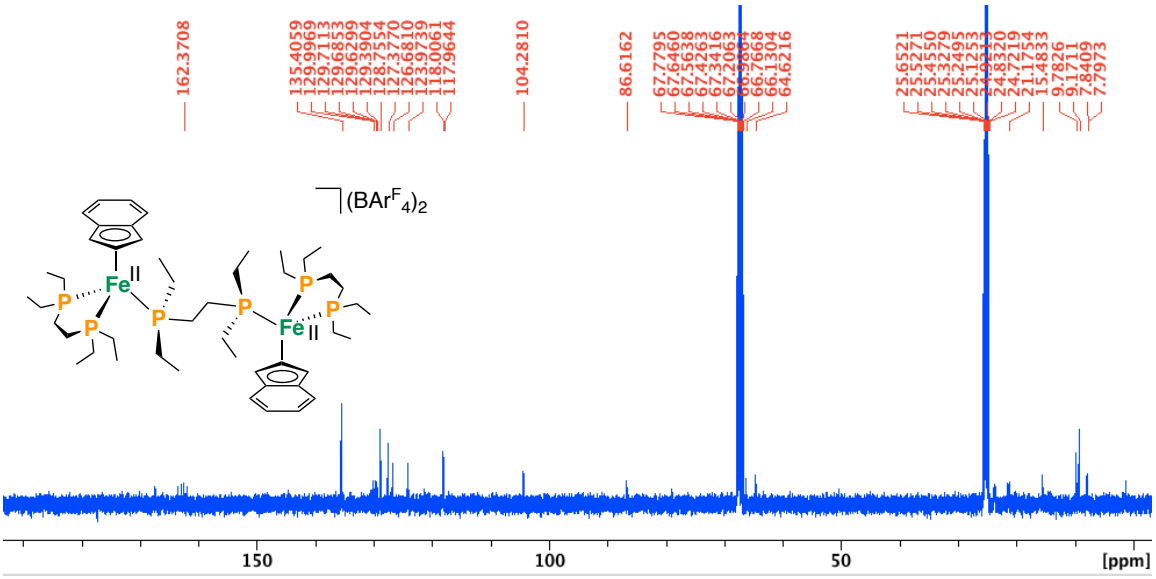

Figure S29. [**7**][BAr^F_4]$_2$, UV-Visible spectrum, THF, 298 K (λ = 329, 491 nm)

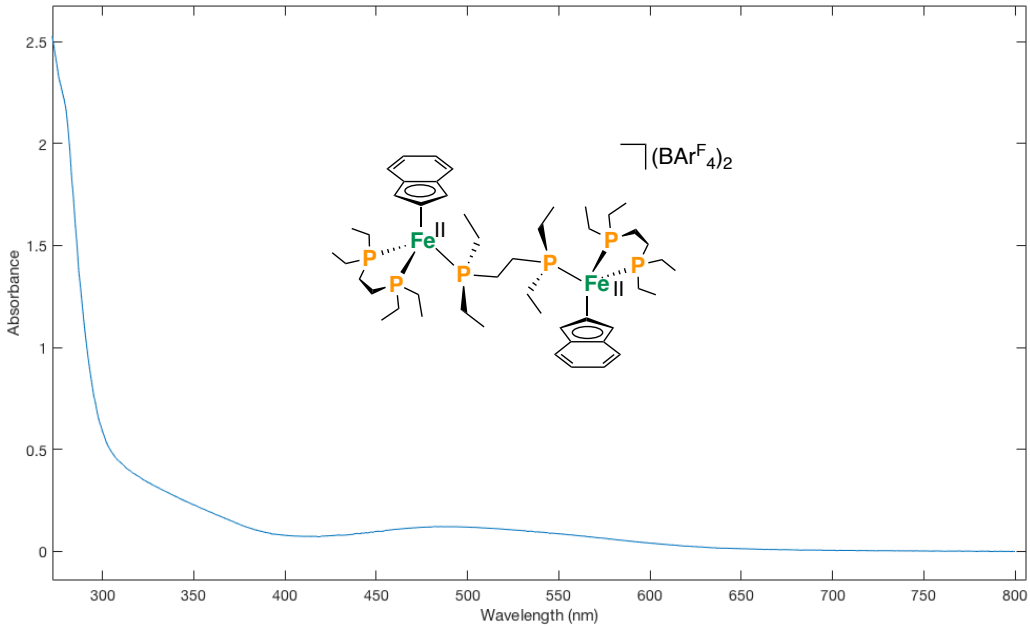

[Fe(η^3:η^2-Ind)(depe)NCCH$_3$][BAr$^F_4$] [8][BAr$^F_4$]: Route A): To a *J. Young* tube containing CD_3CN (500 μL) and **2** was added 1-benzyl-3-acetylpyridinium triflate [BNAP]OTf as a solid; the color changed from red to orange. Analysis by NMR spectroscopy evidenced formation of [Fe(η^3:η^2-Ind)(depe)($NCCH_3$)]OTf and 1,4-BNAPH (~65% by ^{31}P NMR). **Route B)**: To a solution of **2** (4.7 mg, 0.012 mmol, 1 equiv.) in CH_3CN (2 mL) at -35 ˚C was added drop-wise a chilled (-35 ˚C) solution of H(OEt_2)$_2$[BAr$^F_4$] (12.6 mg, 0.012 mmol, 1 equiv.) in CH_3CN (1 mL). Following addition, the resulting mixture was stirred at 25 ˚C over 10 min giving a clear purple solution. Removal of volatiles *in-vacuo* and washing with pentane gave [**8**][BAr$^F_4$] as a purple solid (15.1 mg, 95%).

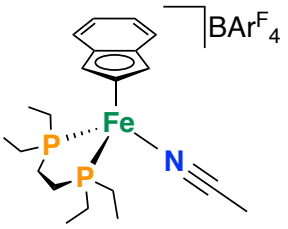

^{1}H NMR (CD_3CN, 400 MHz, 298 K, 1,4-BNAPH): δ = 5.82 (dq, J = 8.1 Hz, J = 1.5 Hz, 1H), 4.86 (dt, J = 8.1 Hz, J = 3.4 Hz, 1H), 4.38 (s, 2H), 2.94 (br s, 2H).

^{1}H NMR (CD_3CN, 400 MHz, 298 K): δ = 7.69 (s, 8H; BAr$^F_4$), 7.67 (s, 4H; BAr$^F_4$), 7.56 (dd, $^3J_{H,H}$ = 6.6 Hz, $^3J_{H,H}$ = 3.1 Hz), 7.27 (dd, $^3J_{H,H}$ = 6.6 Hz, $^3J_{H,H}$ = 3.1 Hz), 4.66 (m, 1H), 4.49 (2H), 2.27 (m, 2H), 1.88 (m, 2H), 1.73 (m, 2H), 1.44 (m, 2H), 1.24 (m, 2H), 1.14 (m, 6H), 0.90 (m, 6H). **^{31}P{^{1}H} NMR (CD_3CN, 162 MHz, 298 K)**: δ = 92.90. **^{13}C NMR (CD_3CN, 100 MHz, 298 K)**: δ = 162.52 (q, $^1J_{C,B}$ = 37 Hz, BAr$^F_4$, ipso quaternary C), 135.61 (BAr$^F_4$, ortho C), 129.86 (q, $^2J_{C,F}$ = 31 Hz, BAr$^F_4$, meta quaternary C), 127.74, 127.25, 125.42 (q, $^1J_{C,F}$ = 273 Hz, BAr$^F_4$, CF_3), 117.97 (m, BAr$^F_4$, para C), 84.98 (η^3:η^2-C_9H_7), 62.17 (η^3:η^2-C_9H_7) 23.29 (m), 21.24 (m), 18.63 (m). **Anal. Calcd.** for $C_{53}H_{46}BF_{24}FeNP_2$ (1281.2): C, 49.67; H, 3.62; N, 1.09. Found: C, 49.30; H, 3.54; N, 1.02.

Figure S30. [**8**][BAr^F_4], ^1H NMR, CD_3CN, 162 MHz, 298 K

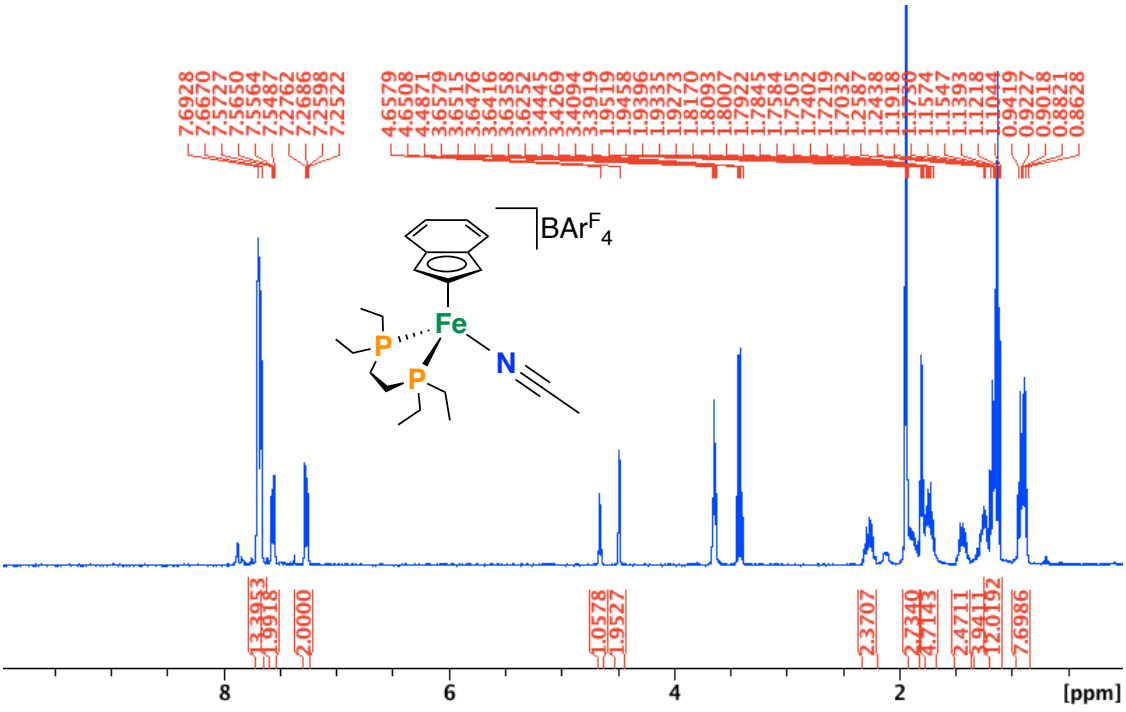

Figure S31. [**8**][BAr^F_4], $^{31}P\{^1H\}$ NMR, CD_3CN, 162 MHz, 298 K

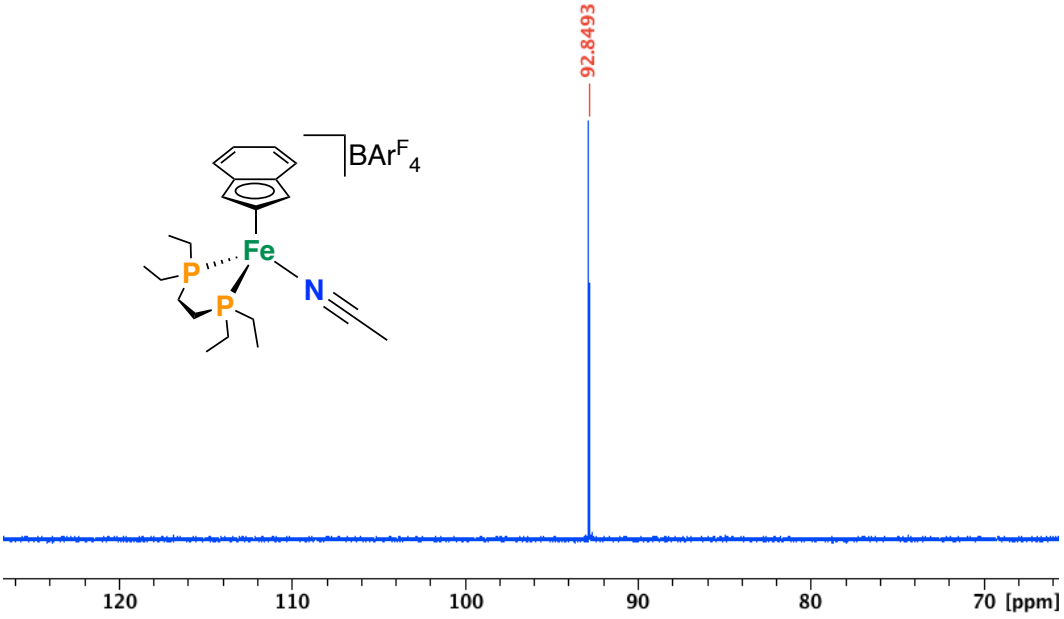

Figure S32. [**8**][BAr^F_4], $^{31}C\{^1H\}$ NMR, CD_3CN, 100 MHz, 298 K

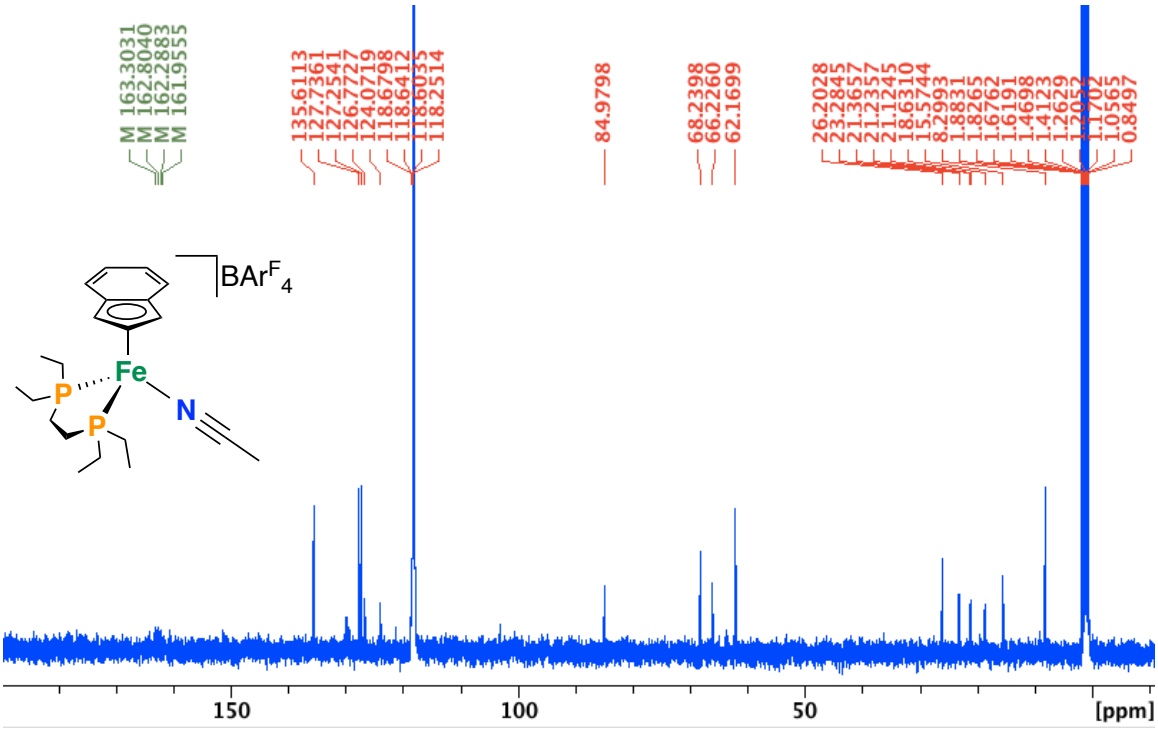

Figure S33. 80 K ^{57}Fe Mössbauer spectrum collected in the presence of a 50 mT magnetic field oriented parallel to the propagation of the γ-beam (frozen solution in 2-MeTHF).

Addition of $[H(OEt_2)_2]BAr^F{}_4$ to **2-^{57}Fe** at -78 °C. Top spectrum shows freeze-quenched sample after 5 min. Bottom spectrum shows freeze-quench after stirring at room temperature for 15 min. Parameters: δ = 0.33 mm/s, ΔE_Q = 1.69 mm/s (**blue, 82%**), δ = 0.14 mm/s, ΔE_Q = 0.29 mm/s (**green, 18%**); $\Gamma_L = \Gamma_R$ = - 0.50 mm/s.

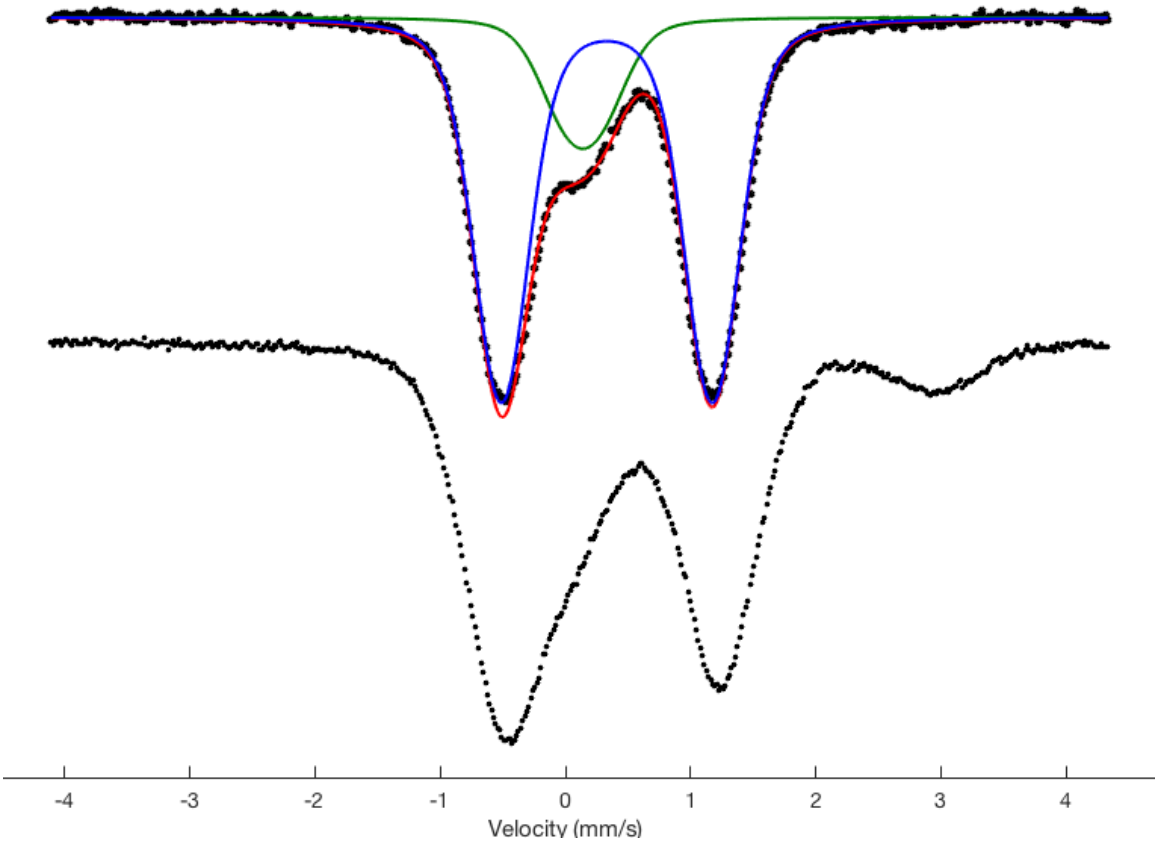

IX. EPR Spectroscopy data:

Figure S34. 77 K X-band EPR spectrum in 2-MeTHF generated by oxidation of **2-H** using [Fc]BAr^{F}_{4} at -78 °C (< 30 s).

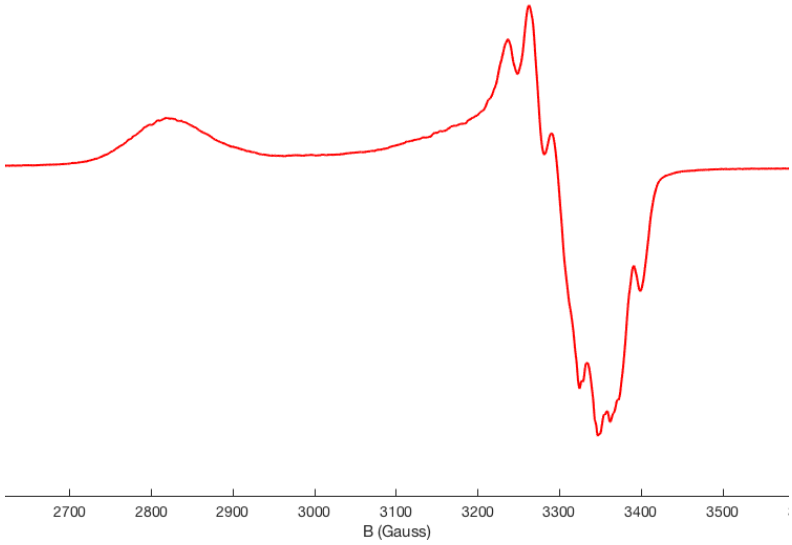

Figure S35. 77 K X-band EPR spectrum in 2-MeTHF generated by oxidation of **2-H** using [Fc]BAr^{F}_{4} at -78 °C, **red** (< 30 s), **blue** (20 min).

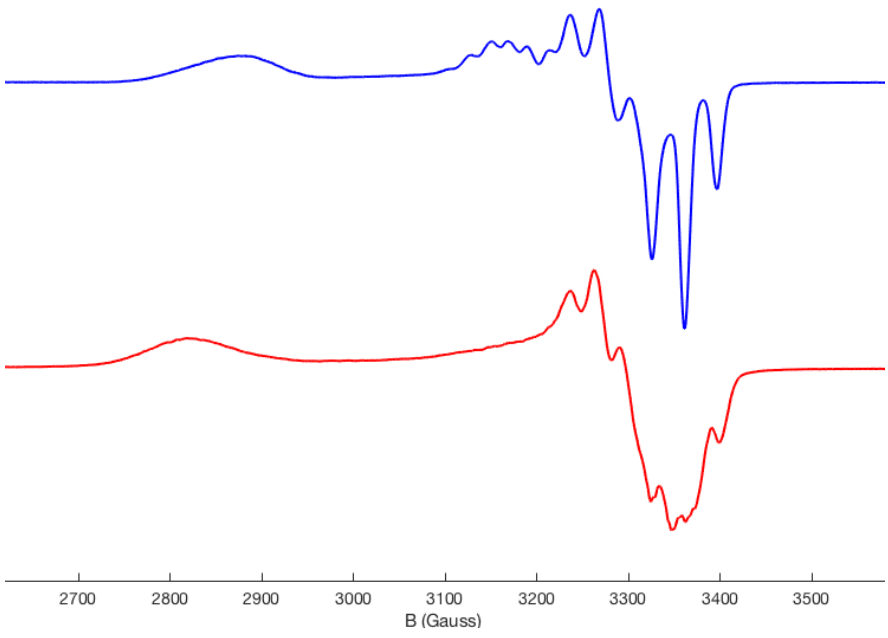

Figure S36. A series of 77 K X-band EPR spectra in 2-MeTHF generated by oxidation of **2-H** using [Fc]BAr^F_4 at -78 °C showing **red** ([**3**]$^+$) giving **green** ([**4**]$^+$), which decomposes to give [Fe^I(depe)N_2]$^+$ (**purple**).

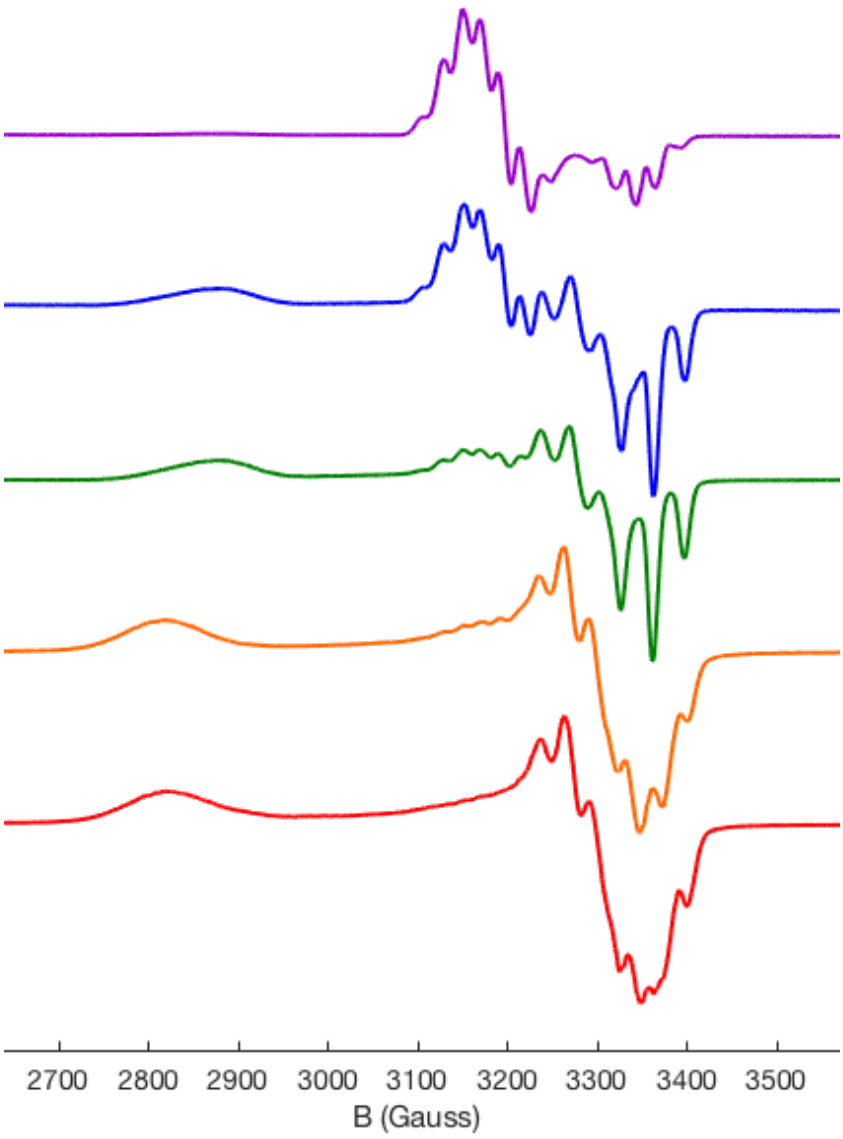

Figure S37. 77 K X-band EPR spectrum of $[Fe^{I}(depe)N_2]^+$ in 2-MeTHF generated by oxidation of **2** using $[Fc]BAr^F_4$ at -78 °C (after 24 h). The fit is consistent with that provided by Ashley[7] and co-workers. Microwave frequency 9.369 GHz; **red** trace: experiment; **blue** trace: simulation. Simulation parameters: Sys.g = [2.125 2.093 2.0016] with four ^{31}P hyperfine interactions, two of type 1, A(^{31}P) = [65.6 61.4 60.9] MHz and two of type 2, A(^{31}P) = [72 61.7 64.3] MHz.

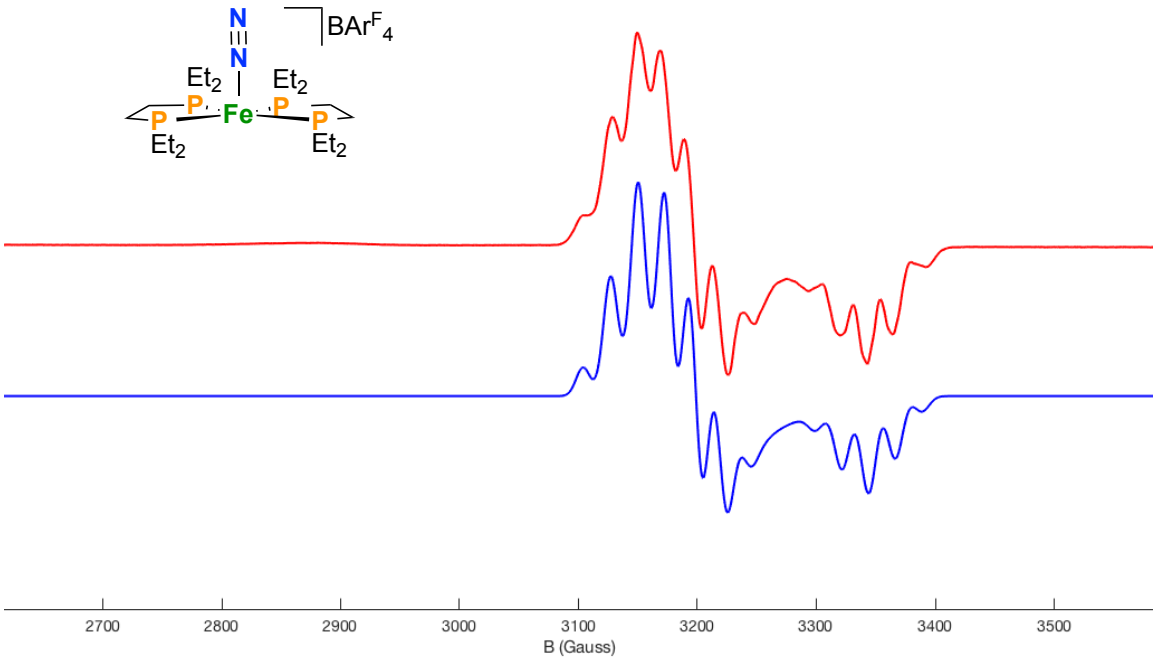

Figure S38. 77 K X-band EPR spectrum in 2-MeTHF generated by oxidation of **2-H** (**red**) and **2-D** (**blue**) using [Fc]BAr^{F}_{4} at -78 °C (< 30 s).

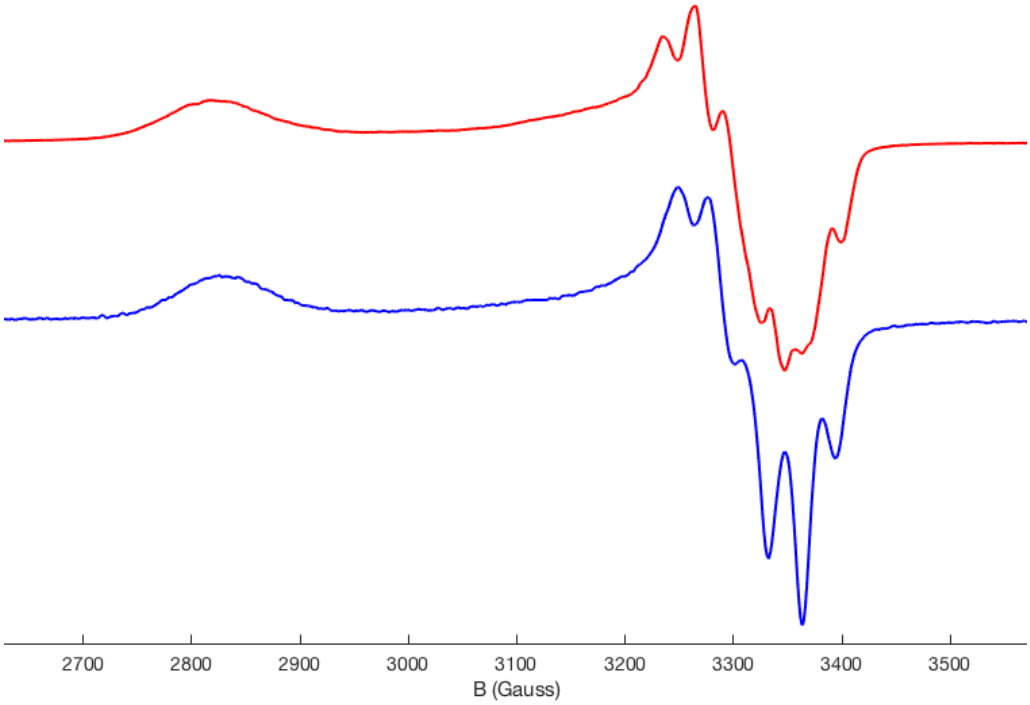

Figure S39. 77 K X-band EPR spectrum in 2-MeTHF generated by oxidation of **2-D** using [Fc]BAr^{F}_{4} at -78 °C **blue** (< 30 s), **red** (20 min).

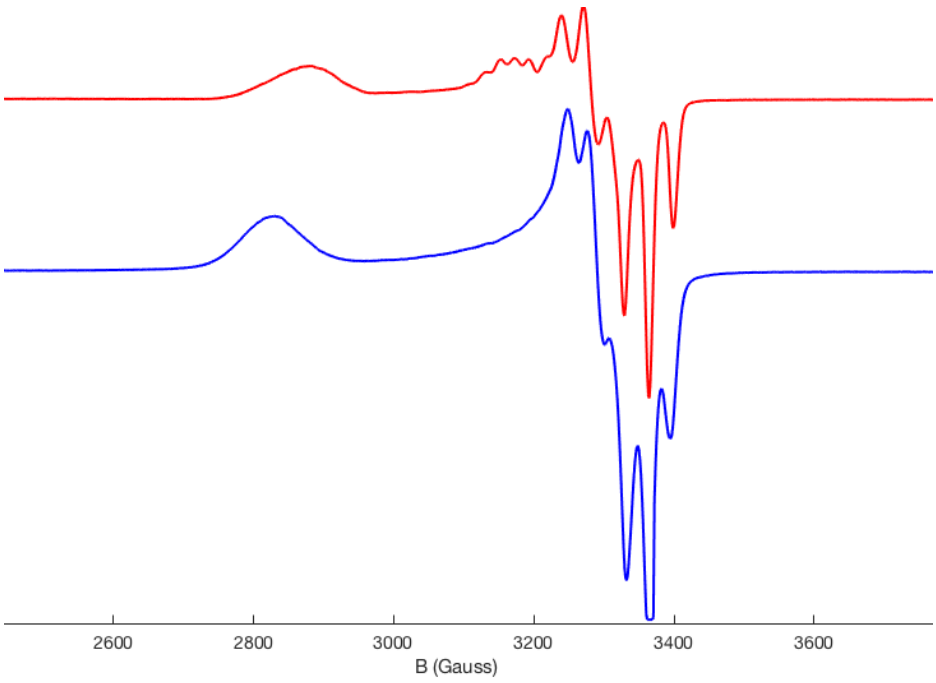

Figure S40. 77 K X-band EPR spectrum in 2-MeTHF generated by oxidation using [Fc]BAr^F_4 at -78 °C of **2-D**: **blue** (< 30 s), **red** (20 min) or **2-H**: **green** (< 30 s), **orange** (20 min) or **2-D** at -78 °C.

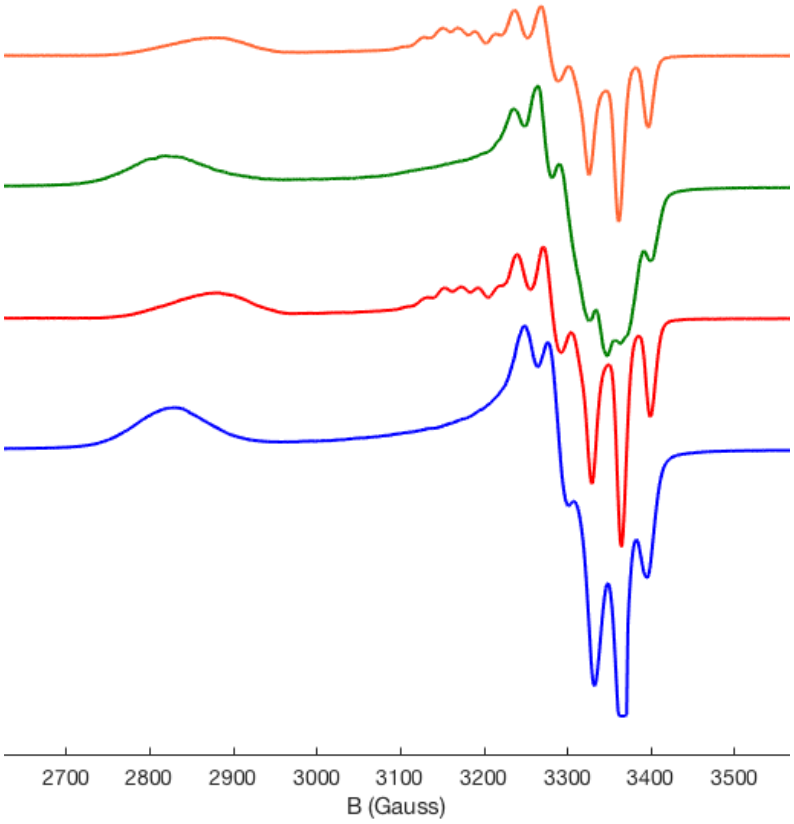

Figure S41. 77 K X-band EPR spectrum of [Fe(η^5-Cp*)(dppe)X]$^+$ (X = H or D) in 2-MeTHF generated by oxidation of the corresponding Fe^{II}-X precursor using [Fc]BAr^F_4 at -78 °C. These spectra show changes at high field, due to coupling of the unpaired electron to a hydride nucleus. For X = D (**blue**), the following fit paramaters were obtained: Sys.g = [2.352, 2.041, 1.992], Sys.lw = 1.2, Sys.Nucs = '^{31}P, ^{31}P', Sys.A = [88, 82, 79; 82, 71, 76], Sys.HStrain = [180 32 31], Exp.mwFreq = 9.370].

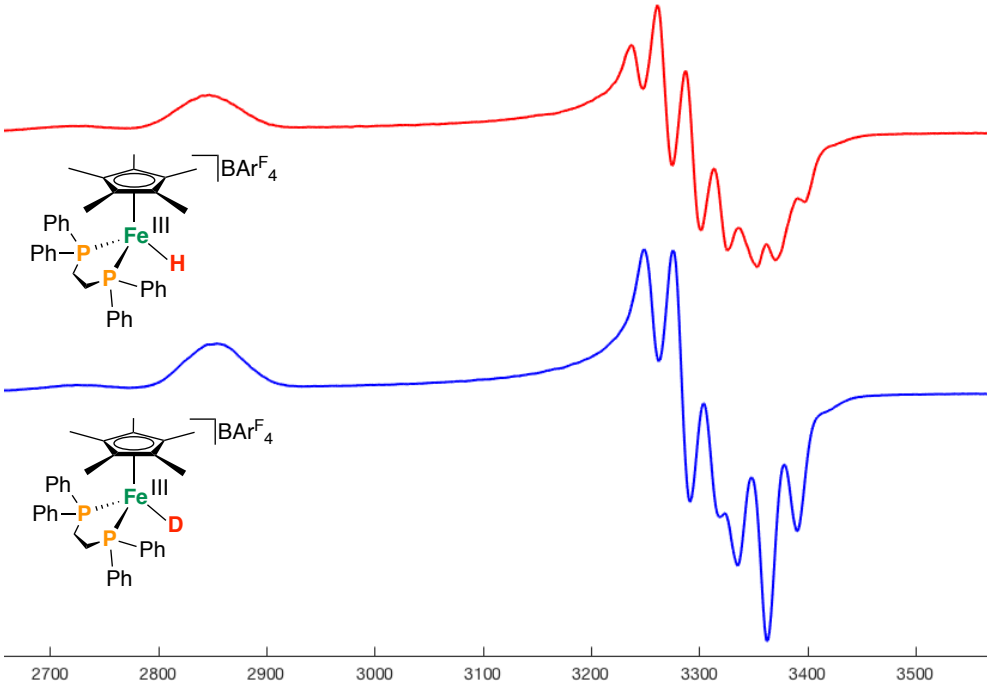

Figure S42. Field-dependent X-band ^{31}P Davies ENDOR of [**3**-D]$^{+}$ (black), with simulations of ^{31}P hyperfine couplings overlaid (total ^{31}P simulation (red), $^{31}P_{\alpha}$, (blue), $^{31}P_{\beta}$ (green)). Simulation parameters: g = [2.377, 2.039, 1.993]; A($^{31}P_{\alpha}$) = [100, 88, 88] MHz, Euler rotation angles [α, β, γ] = [35, 0, 0]$^{\circ}$; A($^{31}P_{\beta}$) = [82, 85, 72] MHz, Euler rotation angles [α,β,γ] = [10, 0, 0]$^{\circ}$. Acquisition parameters: temperature = 10 K; MW frequency = 9.718 GHz; MW pulse length (π/2, π) = 40 ns, 80 ns; RF pulse length = 15 μs; shot repetition time = 2 ms.

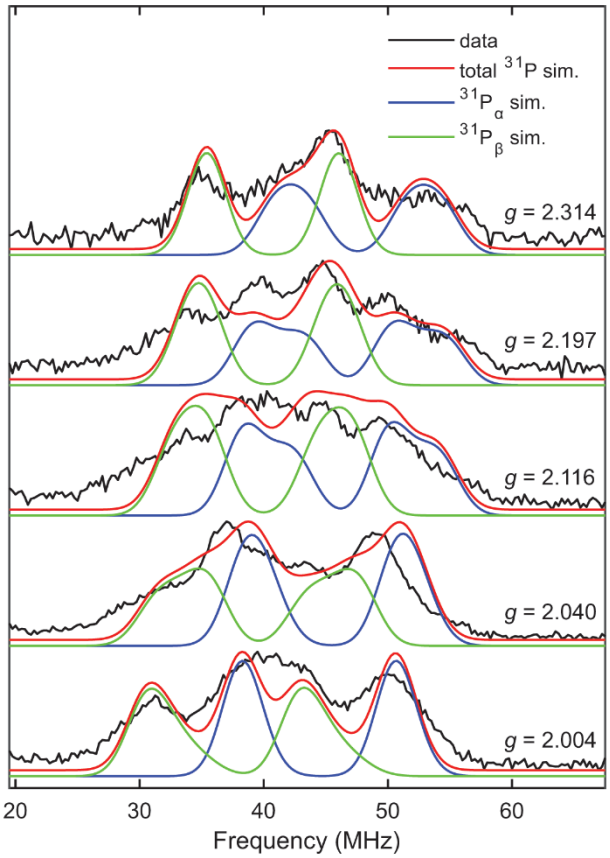

Figure S43. Field-dependent X-band ^{31}P Davies ENDOR of [**4**-D]$^{+}$ (black), with simulations of ^{31}P hyperfine couplings overlaid (total ^{31}P simulation (red), $^{31}P_{\alpha}$, (blue), $^{31}P_{\beta}$ (green)). Simulation parameters: g = [2.332, 2.042, 1.992]; A($^{31}P_{\alpha}$) = [86, 104, 100] MHz, Euler rotation angles [α, β, γ] = [40, 0, 0]$^{\circ}$; A($^{31}P_{\beta}$) = [93, 88, 94] MHz, Euler rotation angles [α,β,γ] = (0, 0, 0)$^{\circ}$. Acquisition parameters: temperature = 10 K; MW frequency = 9.712 GHz; MW pulse length (π/2, π) = 40 ns, 80 ns; RF pulse length = 15 μs; shot repetition time = 2 ms.

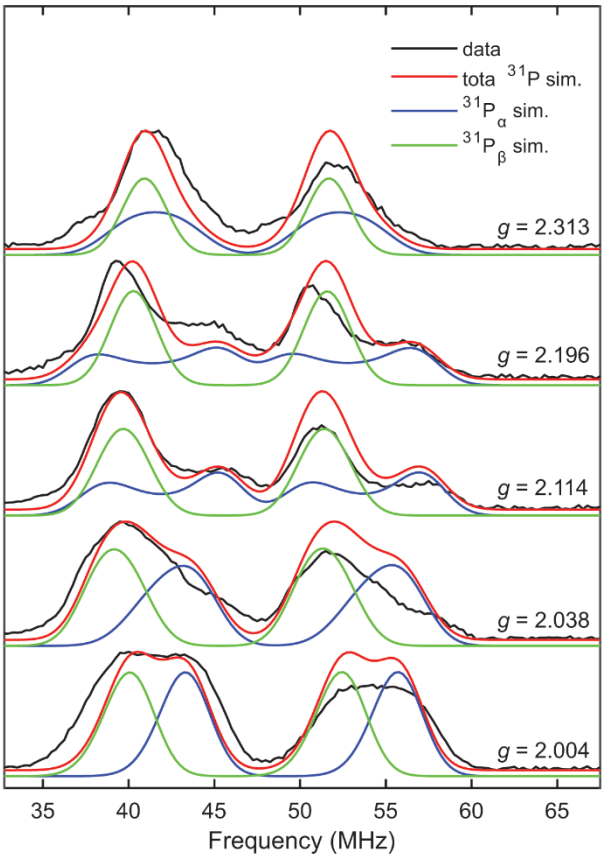

Figure S44. Field-dependent X-band ^{31}P Davies ENDOR of [Fe(η^5-Cp*)(dppe)**D**]$^+$ (black), with simulations of ^{31}P hyperfine couplings overlaid (total ^{31}P simulation (red), $^{31}P_\alpha$, (blue), $^{31}P_\beta$ (green)). Simulation parameters: g = [2.352, 2.041, 1.992]; A($^{31}P_\alpha$) = [88, 82, 79] MHz, Euler rotation angles (α, β, γ) = [0, 0, 0]°; A($^{31}P_\beta$) = [82, 71, 76] MHz, Euler rotation angles (α,β,γ) = [0, 0, 0]°. Acquisition parameters: temperature = 10 K; MW frequency = 9.719 GHz; MW pulse length ($\pi/2$, π) = 40 ns, 80 ns; RF pulse length = 15 μs; shot repetition time = 2 ms.

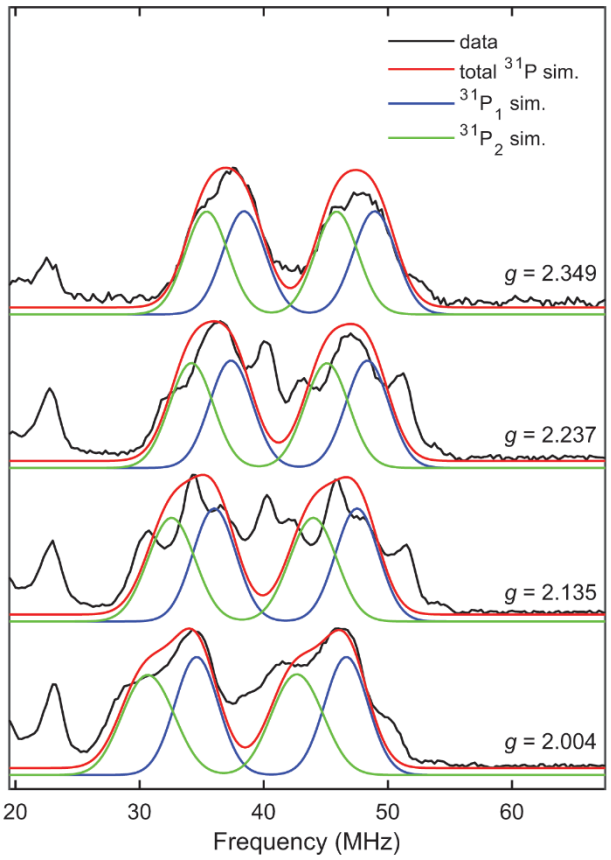

Figure S45. X-band HYSCORE spectra of $[Fe^{I}(depe)N_2]^+$ in 2-MeTHF (top panels) with simulations of features arising from hyperfine couplings to proximal ^{14}N ($^{14}N_p$, red) and distal ^{14}N ($^{14}N_d$, blue) which are consistent with those previously reported by Ashley and co-workers.[7] Simulation parameters: g = [2.125 2.093 2.0016]; A($^{14}N_p$) = [13.6, 13.6, 15.4] MHz, $e^2qQ/h(^{14}N_p)$ = 3.2 MHz, $\eta(^{14}N_p) \approx 0$; A($^{14}N_d$) = [2.7, 2.7, 6.9] MHz, $e^2qQ/h(^{14}N_d)$ = 3.2 MHz, $\eta(^{14}N_d) \approx 0$. Acquisition parameters: temperature = 20 K; microwave frequency = 9.711 GHz; MW pulse length ($\pi/2$, π) = 8 ns, 16 ns; τ = 144 ns (g = 2.114), 138 ns (g = 2.038); $t_1 = t_2$ = 100 ns; $\Delta t_1 = \Delta t_2$ = 16 ns; shot repetition time (srt) = 2 ms.

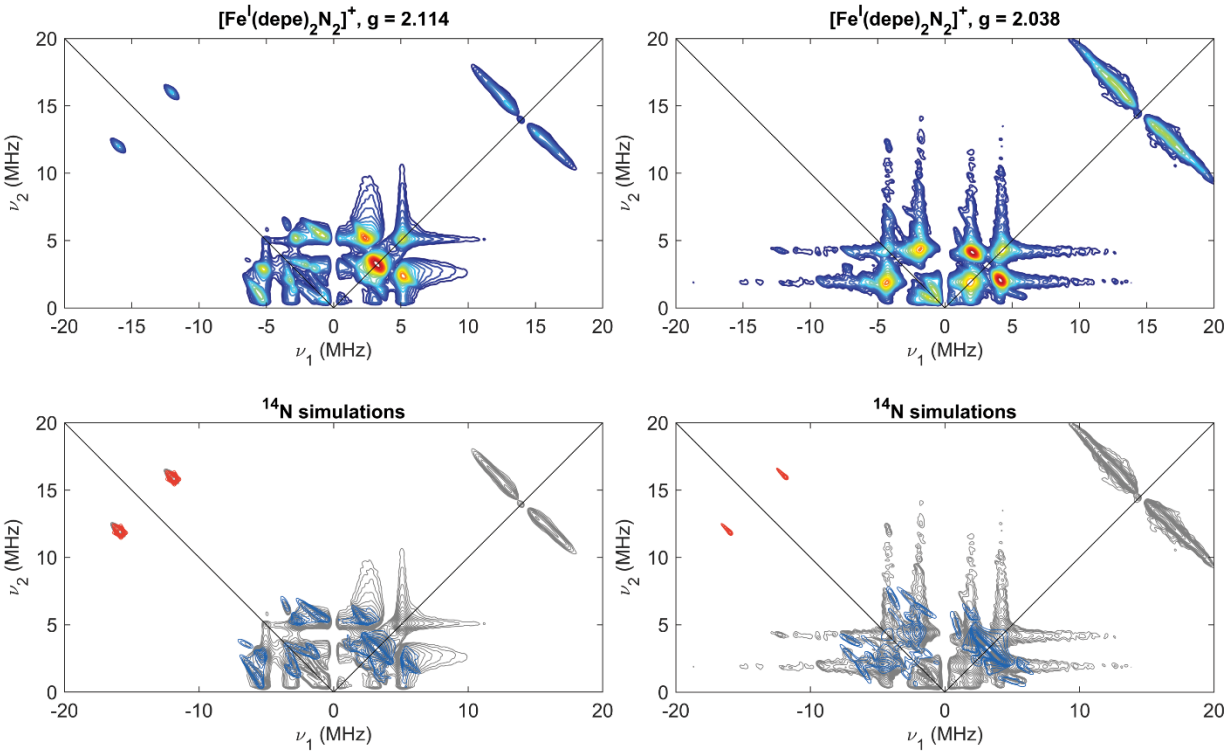

Figure S46. Field-dependent X-band HYSCORE spectra of [**3-H**][BAr^F_4] (top panels) [**3-D**]BAr^F_4 (middle panels) and ^1H-^2H difference HYSCORE spectra (bottom panels). Acquisition parameters: temperature = 10 K; microwave frequency = 9.718 GHz; MW pulse length ($\pi/2$, π) = 8 ns, 16 ns; τ = 156 ns (g = 2.314), 148 ns (g = 2.197); 144 ns (g = 2.116); 138 ns (g = 2.042); $t_1 = t_2$ = 100 ns; $\Delta t_1 = \Delta t_2$ = 16 ns; shot repetition time (srt) = 2 ms.

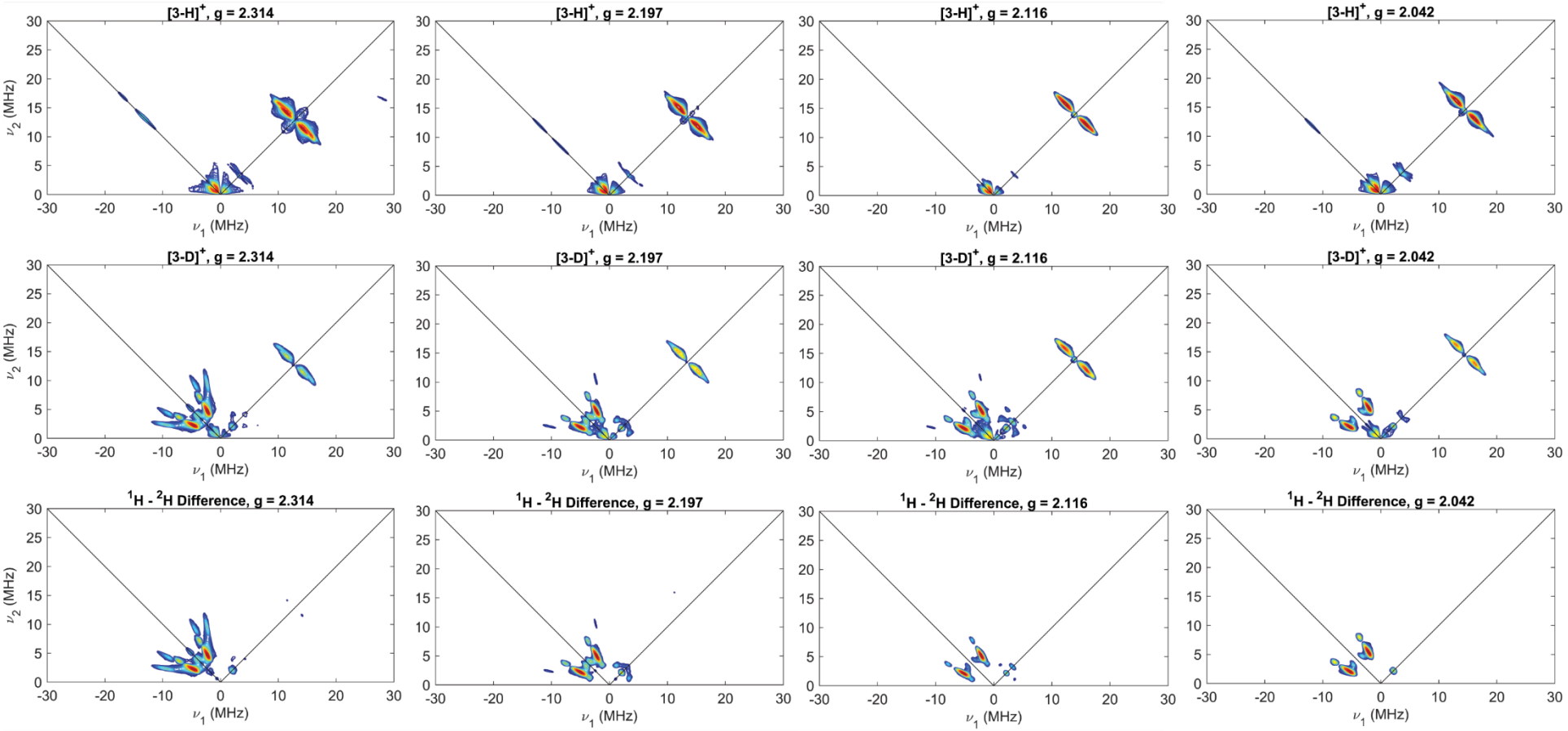

Figure S47. Field-dependent X-band HYSCORE spectra of [**4-H**][BAr^F_4] (top panels) [**4-D**]BAr^F_4 (middle panels) and ^1H-^2H difference HYSCORE spectra (bottom panels). Acquisition parameters: temperature = 10 K; microwave frequency = 9.718 GHz; MW pulse length ($\pi/2$, π) = 8 ns, 16 ns; τ = 156 ns (g = 2.312), 148 ns (g = 2.195); 144 ns (g = 2.111); 138 ns (g = 2.002); $t_1 = t_2 = 100$ ns; $\Delta t_1 = \Delta t_2 = 16$ ns; shot repetition time (srt) = 2 ms.

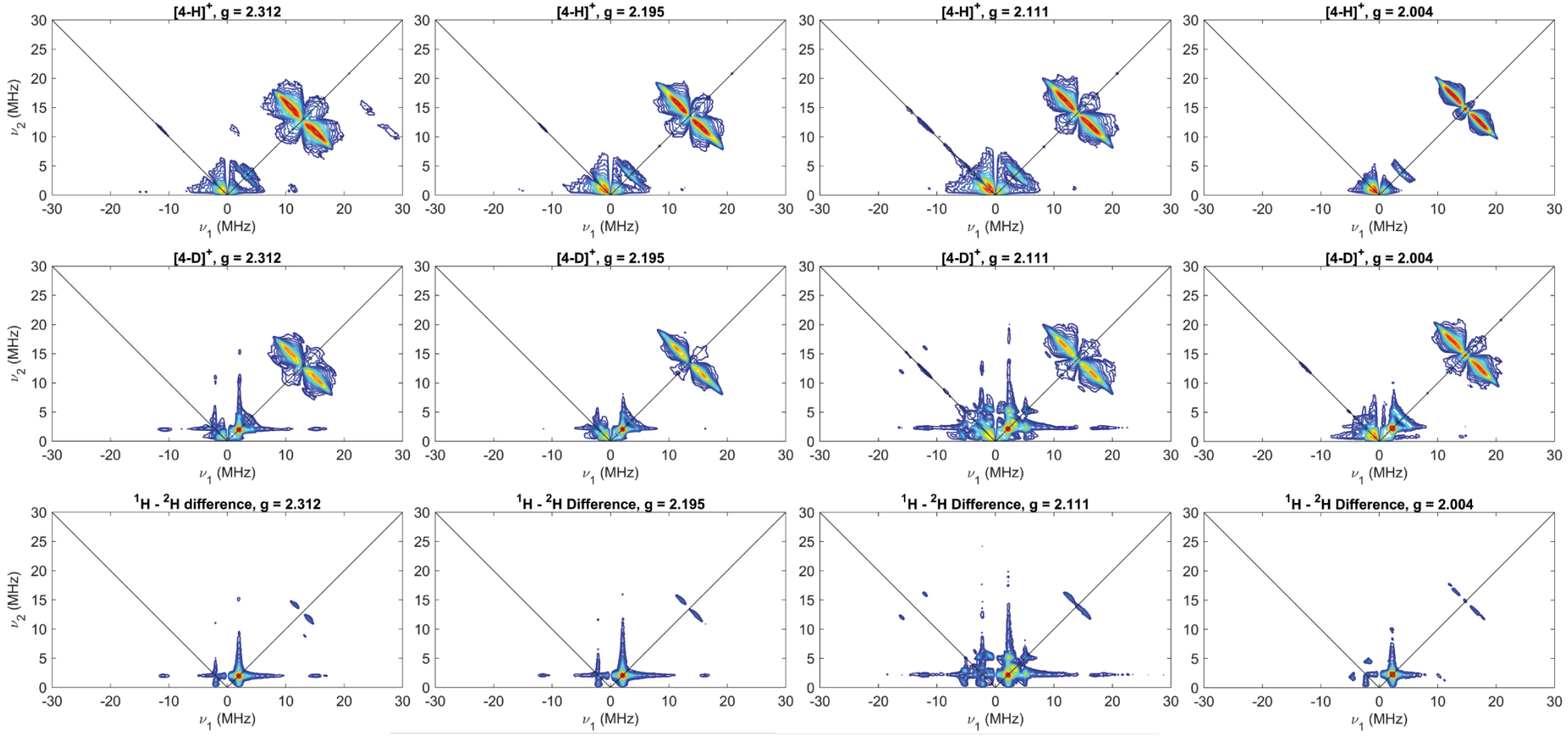

Figure S48. Field-dependent X-band HYSCORE spectra of [**4-H**][BAr^F_4] (top panels) [**4-D**]BAr^F_4 (middle panels) and ^1H-^2H difference HYSCORE spectra (bottom panels) focused on the region in which ^1H features manifest. Acquisition parameters: temperature = 10 K; microwave frequency = 9.718 GHz; MW pulse length ($\pi/2$, π) = 8 ns, 16 ns; τ = 156 ns (g = 2.312), 148 ns (g = 2.195); 144 ns (g = 2.111); 138 ns (g = 2.002); $t_1 = t_2$ = 100 ns; $\Delta t_1 = \Delta t_2$ = 16 ns; shot repetition time (srt) = 2 ms.

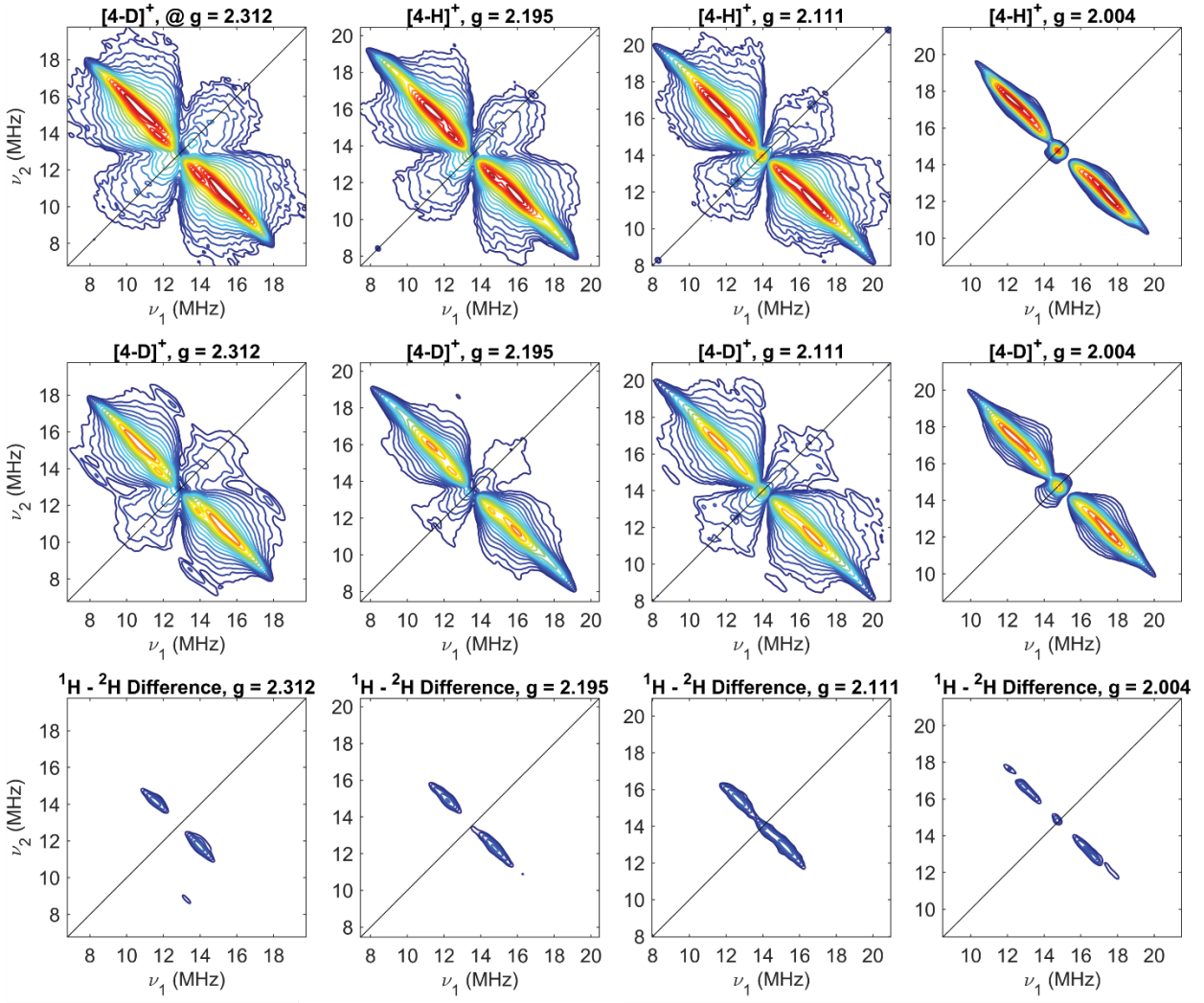

Figure S49. Field-dependent X-band HYSCORE spectra of [Fe^{III}(η^5-Cp*)(dppe)**H**]$^+$ (top panels), [Fe^{III}(η^5-Cp*)(dppe)**D**]$^+$ (middle panels), and ^{1}H-^{2}H difference HYSCORE spectra (bottom panels). Acquisition parameters: temperature = 12 K; microwave frequency = 9.718 GHz; MW pulse length ($\pi/2$, π) = 8 ns, 16 ns; τ = 158 ns (g = 2.349), 152 ns (g = 2.237); 144 ns (g = 2.135); 138 ns (g = 2.042); $t_1 = t_2$ = 100 ns; $\Delta t_1 = \Delta t_2$ = 16 ns; shot repetition time (srt) = 2 ms.

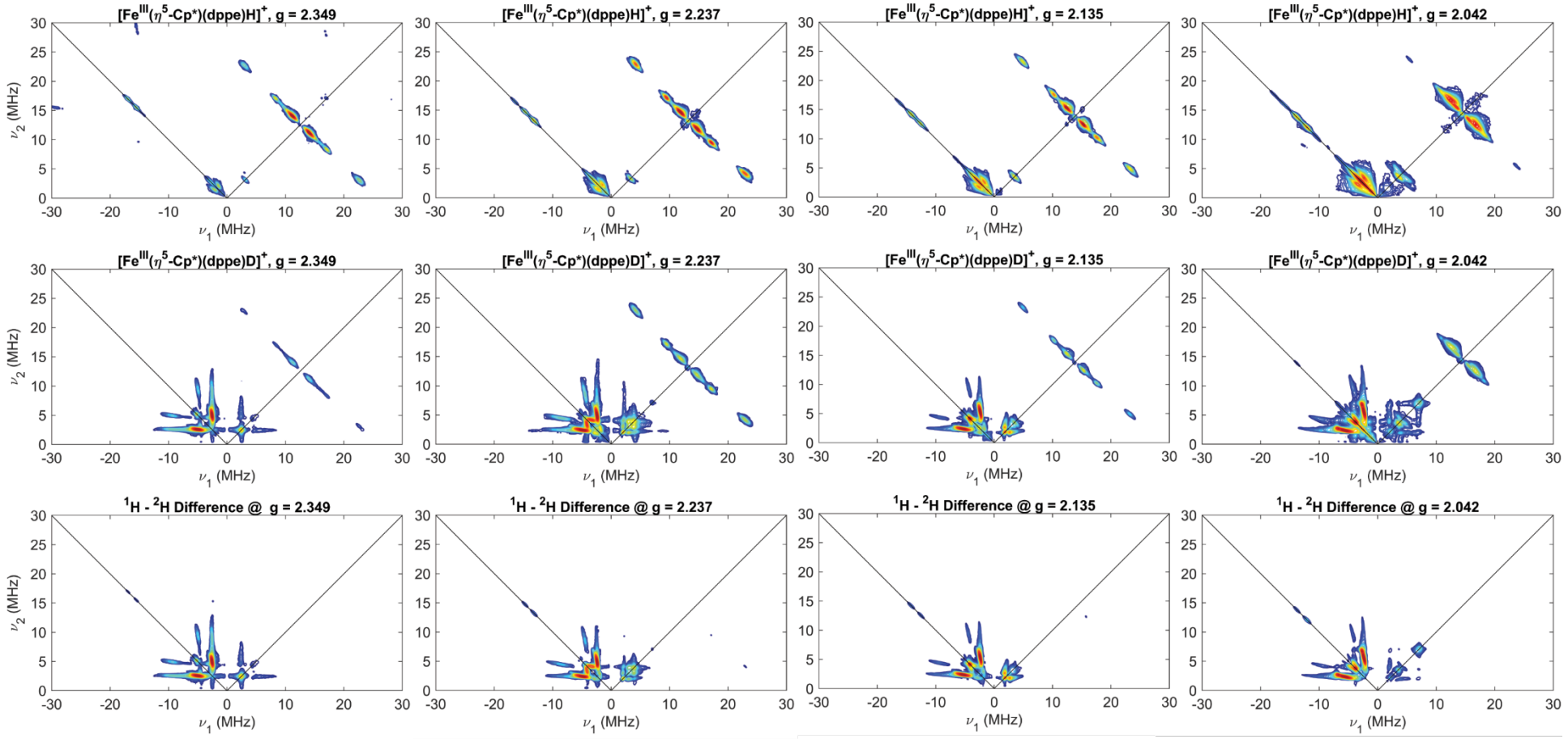

Figure S50. Field-dependent X-band ^{1}H-^{2}H difference HYSCORE spectra of [**3-D**]BAr^{F}_{4} (top panels) and simulations of deuteride ^{2}H features overlaid in red over experimental data displayed in grey (bottom panels). Acquisition parameters: temperature = 10 K; microwave frequency = 9.718 GHz; MW pulse length ($\pi/2$, π) = 8 ns, 16 ns; τ = 156 ns (g = 2.314), 148 ns (g = 2.197); 144 ns (g = 2.116); 138 ns (g = 2.042); $t_1 = t_2$ = 100 ns; $\Delta t_1 = \Delta t_2$ = 16 ns; shot repetition time (srt) = 2 ms.

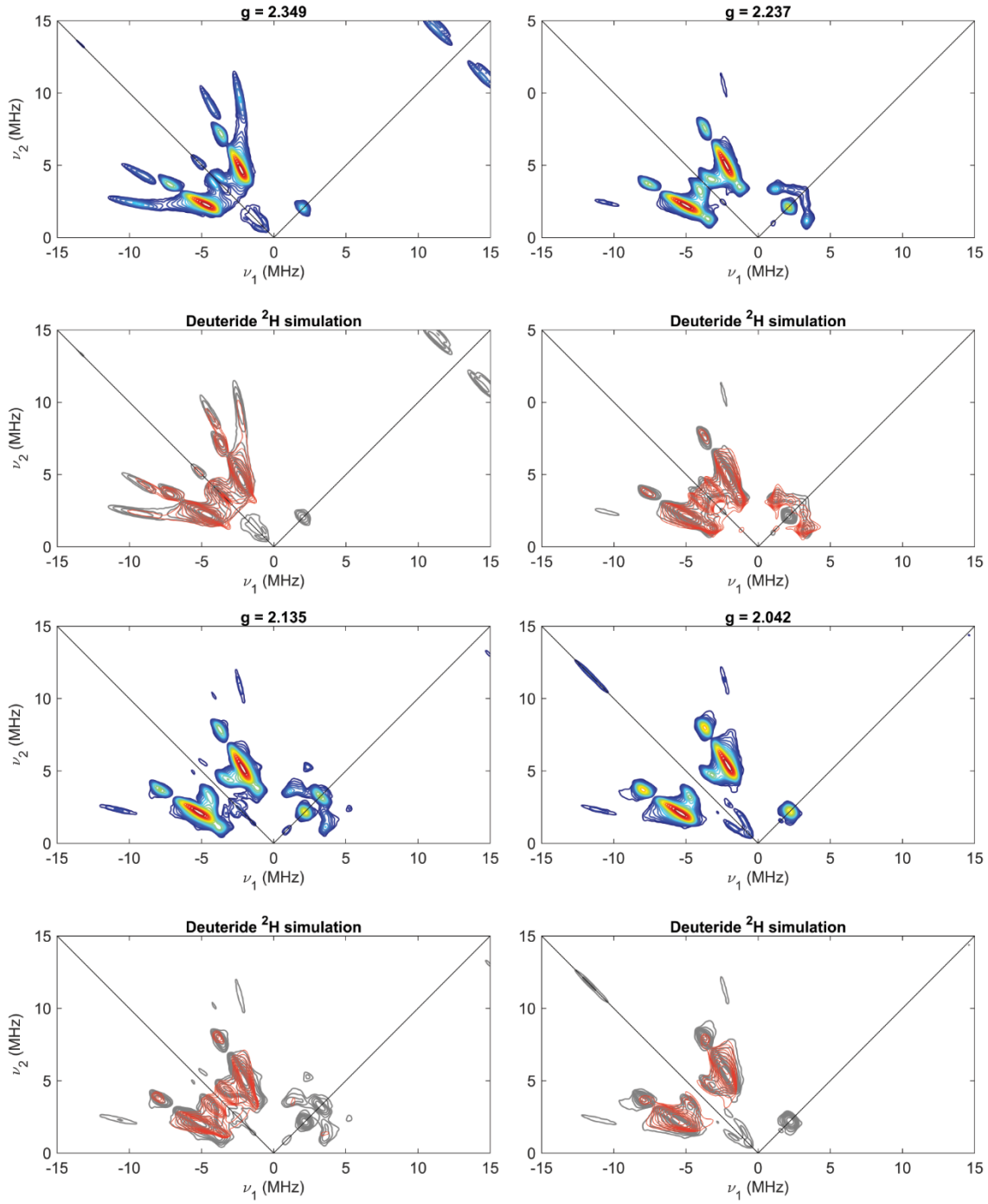

Figure S51. Field-dependent X-band ^{1}H-^{2}H difference HYSCORE spectra of [**4-D**]BAr^{F}_{4} (top panels) and simulations of Indene ^{2}H features overlaid in red over experimental data displayed in grey (bottom panels). Acquisition parameters: temperature = 10 K; microwave frequency = 9.718 GHz; MW pulse length ($\pi/2$, π) = 8 ns, 16 ns; τ = 156 ns (g = 2.312), 148 ns (g = 2.195); 144 ns (g = 2.111); 138 ns (g = 2.002); $t_1 = t_2$ = 100 ns; $\Delta t_1 = \Delta t_2$ = 16 ns; shot repetition time (srt) = 2 ms.

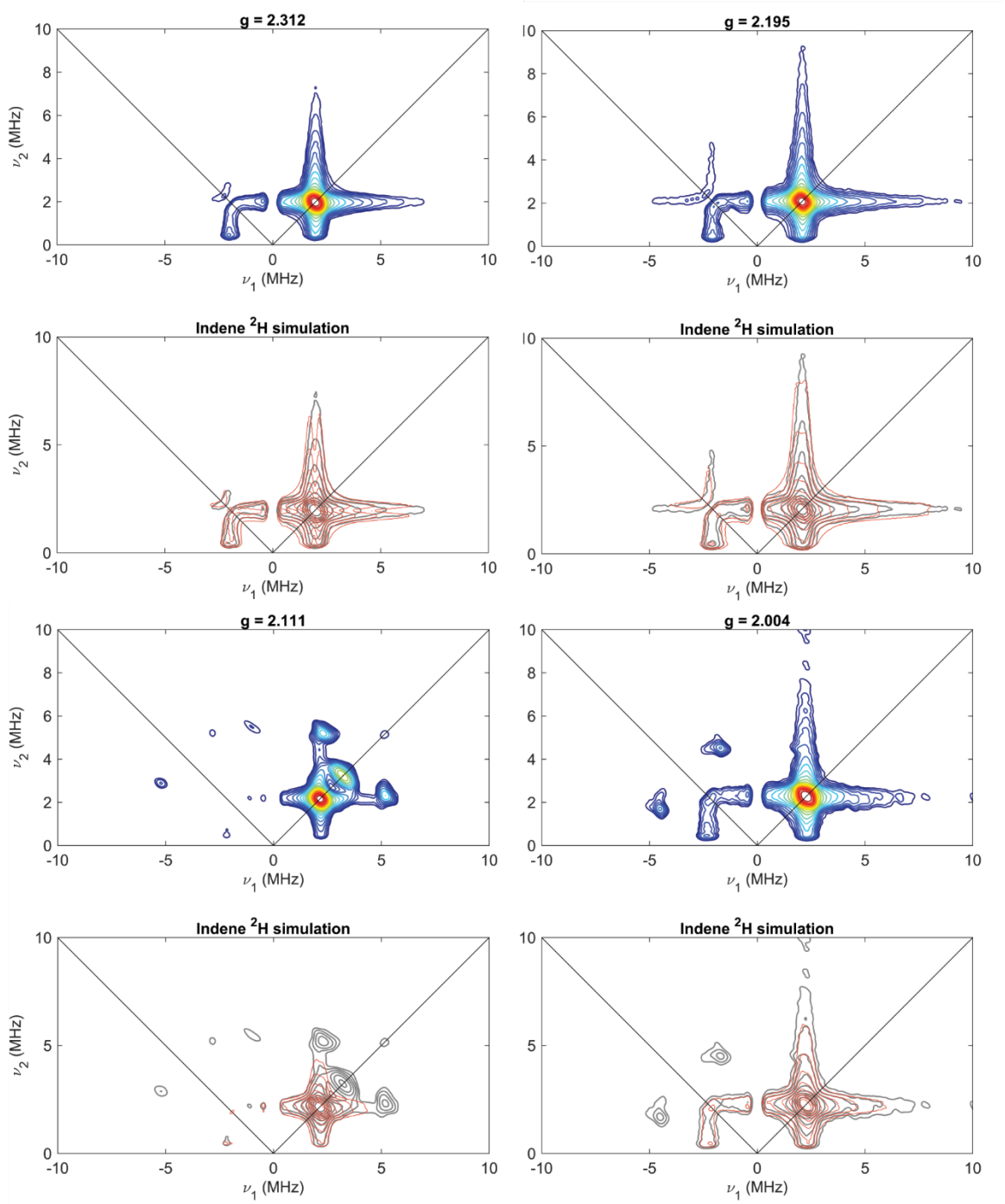

Figure S52. Field-dependent X-band ^{1}H-^{2}H difference HYSCORE spectra of [**4-D**]BAr$^{F}_{4}$ (top panels) and simulations of Indene ^{1}H features overlaid in red over experimental data displayed in grey (bottom panels). Acquisition parameters: temperature = 10 K; microwave frequency = 9.718 GHz; MW pulse length ($\pi/2$, π) = 8 ns, 16 ns; τ = 156 ns (g = 2.312), 148 ns (g = 2.195); 144 ns (g = 2.111); 138 ns (g = 2.002); $t_1 = t_2$ = 100 ns; $\Delta t_1 = \Delta t_2$ = 16 ns; shot repetition time (srt) = 2 ms.

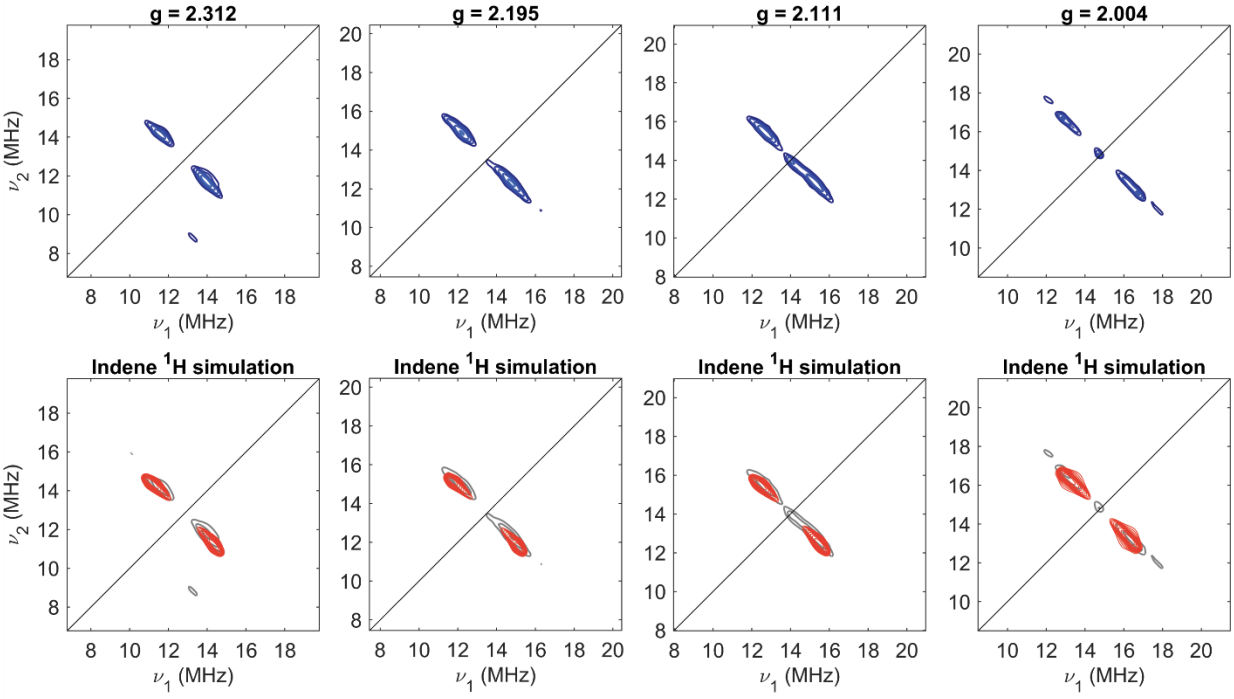

Figure S53. Field-dependent X-band ^{1}H-^{2}H difference HYSCORE spectra of [Fe^{III}(η^5-Cp*)(dppe)**D**]$^{+}$ (top panels) and simulations of deuteride ^{2}H features overlaid in red over experimental data displayed in grey (bottom panels). Acquisition parameters: temperature = 12 K; microwave frequency = 9.718 GHz; MW pulse length ($\pi/2$, π) = 8 ns, 16 ns; τ = 158 ns (g = 2.349), 152 ns (g = 2.237); 144 ns (g = 2.135); 138 ns (g = 2.042); $t_1 = t_2$ = 100 ns; $\Delta t_1 = \Delta t_2$ = 16 ns; shot repetition time (srt) = 2 ms.

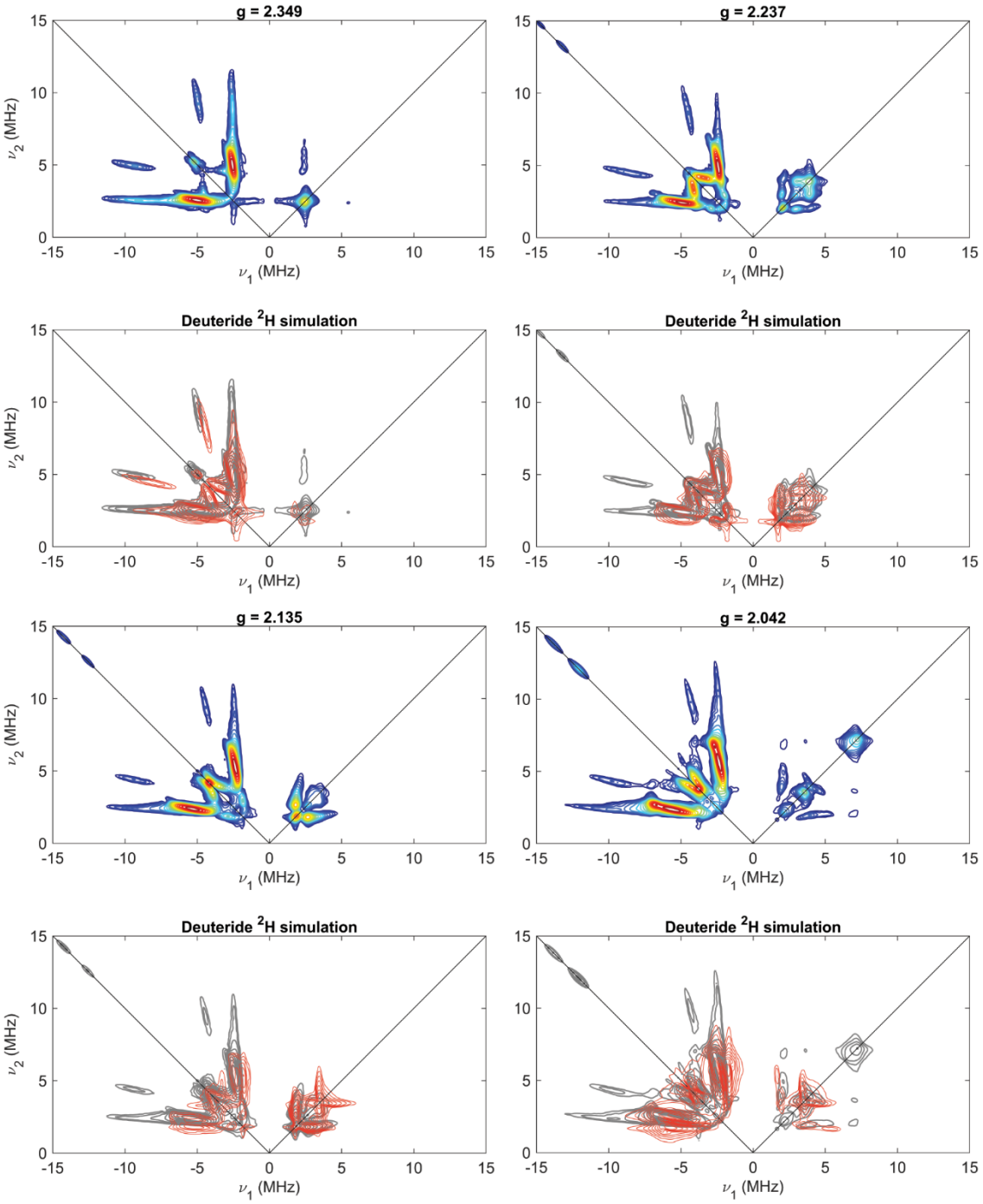

X. Rate Data:

Figure S54. UV-VIS spectrum showing decay of [**3**]$^+$ to give [**4**]$^+$ at -60 °C in 2-MeTHF.

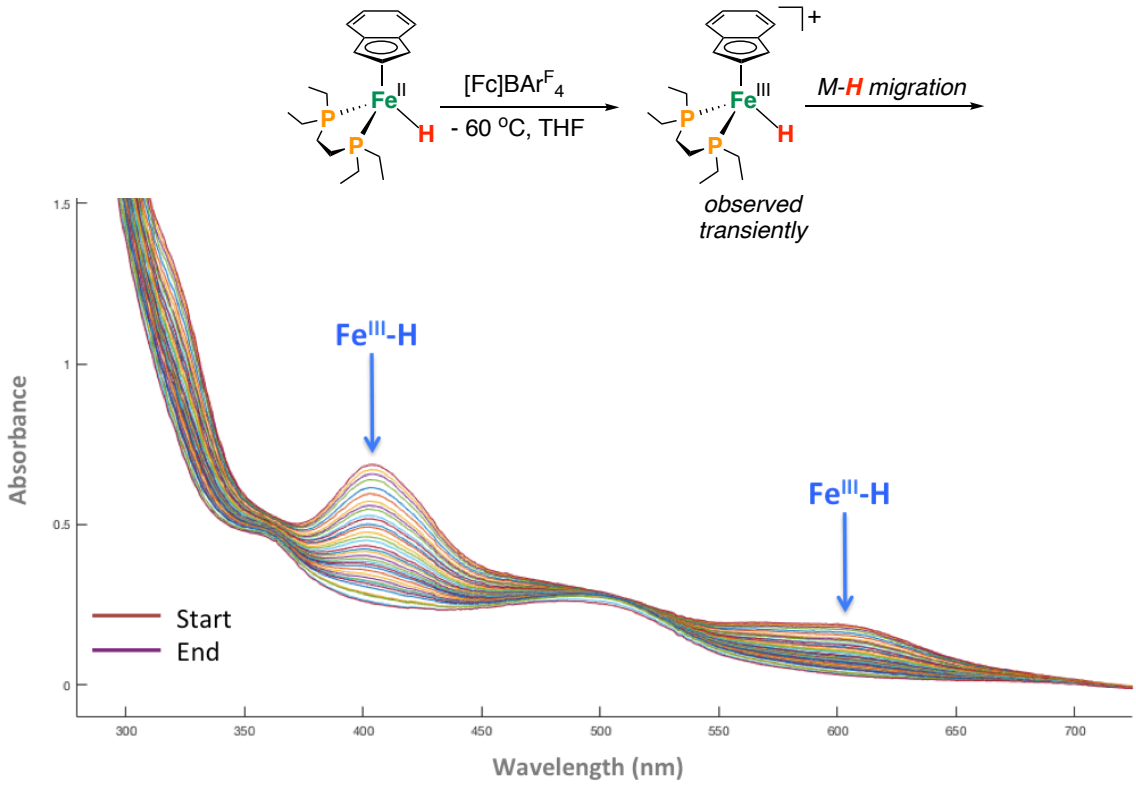

Figure S55. Reaction monitoring at λ = 404 nm showing decay of $[\mathbf{3}]^+$ at -60 ºC in 2-MeTHF.

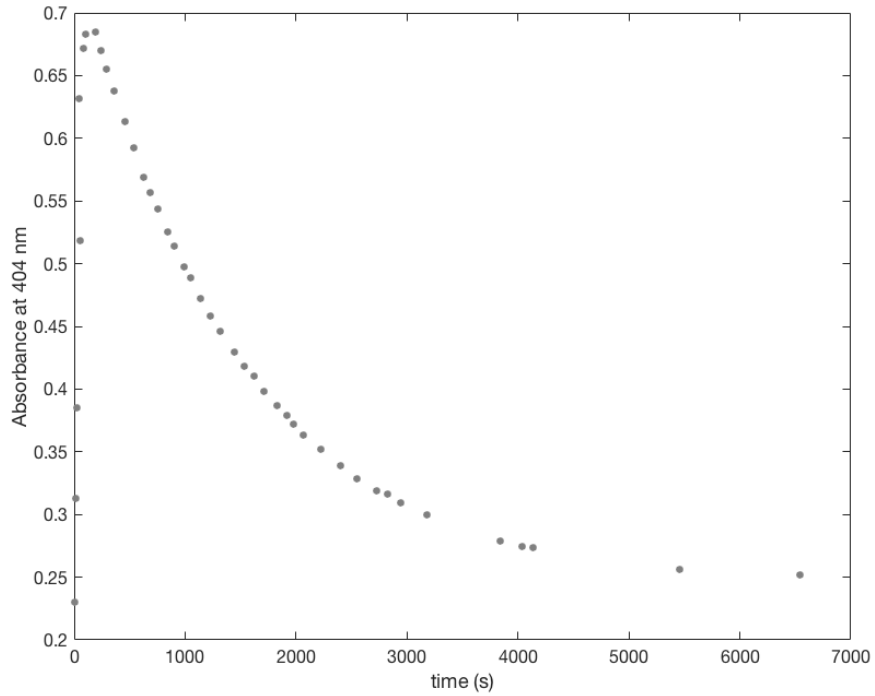

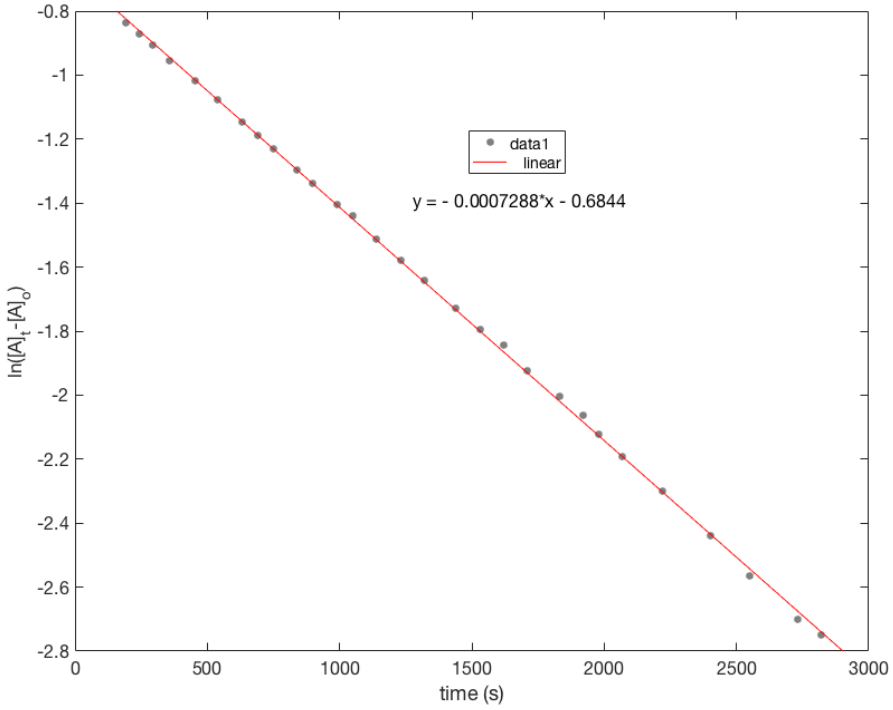

XI. Crystallographic details:

All crystals were mounted on a glass fiber loop. All measurements were made using graphite-monochromated Mo or Cu K_α radiation (λ = 0.71073 or 1.54178 Å) on a Bruker AXS D8 VENTURE KAPPA diffractometer coupled to a PHOTON 100 CMOS detector. The structures were solved by direct methods[8] and refined by full-matrix least-squares procedures on F2 (SHELXL-2013)[6] using the OLEX2 interface.[9] All hydrogen atoms were placed in calculated positions. Non-hydrogen atoms were refined anisotropically.

1: This crystal is a twin. The following twin law was obtained: **TWIN LAW** (-1.0, 0.0, 0.0, 0.0, 1.0, 0.0, 0.0, 0.0, -1.0, 2.0), **BASF** [0.562(6)] using OLEX2; this led to improved data statistics.

4: This crystal features disorder about an entire depe ligand that was modeled as a 41:59 split; this led to improved data statistics.

[**5**][BAr^F_4]: A q-peak near Fe was assigned as a partially occupied Fe site (PLAT307). Q-peaks for the remainder of the Fe-containing molecule were not observed, due to the degree of disorder being relatively small. PLAT971 suggested that there was residual electron density, however, this is not attributable to an atom. The electron density appears near a phenyl ring and Fe.

[**6**][BAr^F_4]: One side of the depe ligand was modeled in two orientations in a 38/62 split C16/C17/C20/C21 [38] and C18/C19/C22/C23 [62]; this led to improved data statistics. [**7**][$BAr^F_4]_2$: This crystal contains a disordered pentane molecule located on an inversion center (this was not modeled).

CCDC **1896047-1896051** contains the supplementary crystallographic data for this paper. These data can be obtained free of charge from The Cambridge Crystallographic Data Centre via www.ccdc.cam.ac.uk/data_request/cif

Table S1. Crystallographic data for **1**, **4**, [**5**][BAr^F_4], and [**6**][BAr^F_4].

Compound	**1**	**4**	[**5**][BAr^F_4]	[**6**][BAr^F_4]
Empirical formula	$C_{19}H_{31}BrFeP_2$	$C_{51}H_{44}BF_{24}FeP_2$	$C_{53}H_{52}BF_{24}FeP_2$	$C_{56}H_{52}BF_{24}FeN_2P_2$
Formula weight	457.14	1241.46	1273.54	1337.59
Temperature/K	100(2)	100(2)	100(2)	100(2)
Crystal system	Orthorhombic	Monoclinic	Monoclinic	Monoclinic
Space group	$Pna2_1$	$P2_1/c$	$P2_1/c$	$P2_1/n$
a/Å	15.4701(4)	11.9688(6)	17.9424(6)	16.4173(6)
b/Å	17.1275(5)	17.5103(11)	17.3777(5)	16.3342(5)
c/Å	7.5971(2)	24.9005(16)	19.0513(6)	22.0278(8)
α/°	90	90	90	90
β/°	90	95.858(2)	111.447(2)	91.9240(10)
γ/°	90	90	90	90
V/Å^3	2012.96(9)	5191.3(5)	5528.8(3)	5903.7(4)
Z	4	4	4	4
ρ/ g/cm^{-3}	1.508	1.588	1.530	1.505
μ/ mm^{-1}	2.891	0.475	3.802	0.425
F(000)	944.0	2508.0	2588.0	2716.0
Crystal size/ mm^3	0.18 × 0.18 × 0.16	0.23 × 0.17 × 0.17	0.38 × 0.29 × 0.23	0.28 × 0.2 × 0.17
Radiation	MoKα (λ = 0.71073)	MoKα (λ = 0.71073)	CuKα (λ = 1.54178)	MoKα (λ = 0.71073)
2θ range for data collection/°	4.756 to 54.994	4.498 to 52.878	5.292 to 147.104	4.462 to 55.826
Index ranges	$-20 \le h \le 20$, $-22 \le k \le 22$, $-9 \le l \le 9$	$-14 \le h \le 14$, $-21 \le k \le 21$, $-31 \le l \le 31$	$-21 \le h \le 22$, $-20 \le k \le 21$, $-23 \le l \le 23$	$-21 \le h \le 21$, $-21 \le k \le 21$, $-29 \le l \le 29$
Independent reflections	4612 [R_{int} = 0.0752, R_{sigma} = 0.0242]	10453 [R_{int} = 0.1878, R_{sigma} = 0.1618]	11079 [R_{int} = 0.0572, R_{sigma} = 0.0199]	14128 [R_{int} = 0.0849, R_{sigma} = 0.0379]
Data/restraints/parameters	4612/1/213	10453/912/866	11079/729/744	14128/786/821
Goodness-of-fit on F^2	1.046	0.995	1.051	1.014
R [I>=2θ (I)] (R1, wR2)	R_1 = 0.0175, wR_2 = 0.0432	R_1 = 0.0828, wR_2 = 0.2121	R_1 = 0.0995, wR_2 = 0.2894	R_1 = 0.0744, wR_2 = 0.1872
R (all data) (R1, wR2)	R_1 = 0.0189, wR_2 = 0.0439	R_1 = 0.1053, wR_2 = 0.2400	R_1 = 0.1122, wR_2 = 0.3046	R_1 = 0.1060, wR_2 = 0.2106
Largest diff. peak/hole / (e Å^{-3})	0.27/-0.32	1.01/-0.48	4.25/-1.24	1.26/-0.97

$R1 = \Sigma \, ||F_o|-|F_c|| \, / \, \Sigma \, |F_o|$; $wR2 = [\Sigma(w(F_o^2 - F_c^2)^2) \, / \, \Sigma \, w(F_o^2)^2]^{1/2}$

Table S2. Crystallographic data for [**7**][BAr^{F}_{4}]$_2$.

Compound	[**7**][BAr^{F}_{4}]$_2$
Empirical formula	$C_{60}H_{55}BF_{24}FeP_3$
Formula weight	1391.61
Temperature/K	100(2)
Crystal system	Triclinic
Space group	P-1
a/Å	12.5836(7)
b/Å	13.0412(7)
c/Å	19.6731(11)
α/°	103.588(2)
β/°	106.523(2)
γ/°	90.595(2)
V/Å^3	2998.2(3)
Z	2
ρ/ g/cm^{-3}	1.541
μ/ mm^{-1}	0.446
F(000)	1414.0
Crystal size/ mm^3	0.71 × 0.22 × 0.16
Radiation	MoKα (λ = 0.71073)
2θ range for data collection/°	4.352 to 70.178
Index ranges	-20 ≤ h ≤ 20, -20 ≤ k ≤ 18, -30 ≤ l ≤ 28
Independent reflections	19818 [R_{int} = 0.0368, R_{sigma} = 0.0568]
Data/restraints/parameters	19818/0/808
Goodness-of-fit on F^2	1.051
R [I>=2θ (I)] (R1, wR2)	R_1 = 0.0546, wR_2 = 0.1311
R (all data) (R1, wR2)	R_1 = 0.0853, wR_2 = 0.1533
Largest diff. peak/hole / (e Å^{-3})	0.78/-0.77

$R1 = \Sigma \, ||F_o|-|F_c|| \, / \, \Sigma \, |F_o|$; $wR2 = [\Sigma(w(F_o^2 - F_c^2)^2) \, / \, \Sigma \, w(F_o^2)^2]^{1/2}$

Table S3. Summary of data obtained from X-ray analyses

	1	[**4**][BAr^F_4]	[**5**][BAr^F_4]	[**6**][BAr^F_4]	[**7**][BAr^F_4]$_2$
Spin-state	$S = 0$	$S = ½$	$S = ½$	$S = 0$	$S = 0$
o.s.	2+	1+	1+	2+	2+
d(Fe-P1) (Å)	2.1792(6)	2.222(3)	2.254(2)	2.208(1)	2.1960(7)
d(Fe-P2) (Å)	2.2217(6)	2.298(3)	2.272(2)	2.206(1)	2.2413(7)
Ω	4.58	-	-	4.30	6.02
Δ(M-C)	0.134	-	-	0.089	0.134
ϕ 127.5	90	96.7	127.5	135.1	

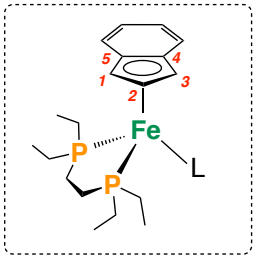

ϕ = angle between the two planes made by P1,Fe1,P2 and C1, C2, C3, C4, C5

Δ(M-C) = average of d(Fe-C1, Fe-C2, Fe-C3) minus average of d(Fe-C4, Fe-C5)

Ω = angle between the two planes made by C1, C2, C3 and C1, C5, C4, C3 [envelope angle]

XII. DFT Calculations:

General:

Geometry optimizations were performed using Gaussian 09 [Rev. A.02][10] at the following level of theory: TPSS functional,[11] a def2-TZVP basis set on iron and a def2-SVP basis set on all other atoms.[12] Frequency calculations were used to confirm true minima and to determine gas phase free energy values (G_{gas}).

$BDFE_{X-H}$ Calculations:

Consistent with a previous report, a calibration curve of ΔG vs. $BDFE_{lit}$ was employed.[13] The free-energy difference between the H-atom donor/acceptor pair was calculated based on the thermochemical information provided by frequency calculations after structure optimizations using the procedure described in the general computational section.

^{57}Fe Mössbauer Calculations:

The ^{57}Fe Mössbauer isomer shifts in Table S4 have been calculated using the extended calibration parameters according to Neese.[14] Isomer shifts were calculated according to the equation $\delta_{calc} = \alpha(\rho(0)-C+\beta$, with $\alpha = -0.17683$, $\beta = 0.35964$ and $C = 23600$.[9] Taking the systematic overestimation of this method into account, this provides a good indication of the isomer shifts. In contrast, the older set of calibration parameters[15] (not included in Table S4) underestimate the observed isomer shifts.

Figure S56. Free energy change (kcal mol^{-1}) for PCET from the η^4-dienyl complex, involving BDFE$_{C\text{-}H}$ (TPSS; def2tzvp (Fe), def2svp (all other atoms)). ΔG^o_{HAA} = hydrogen atom affinity.

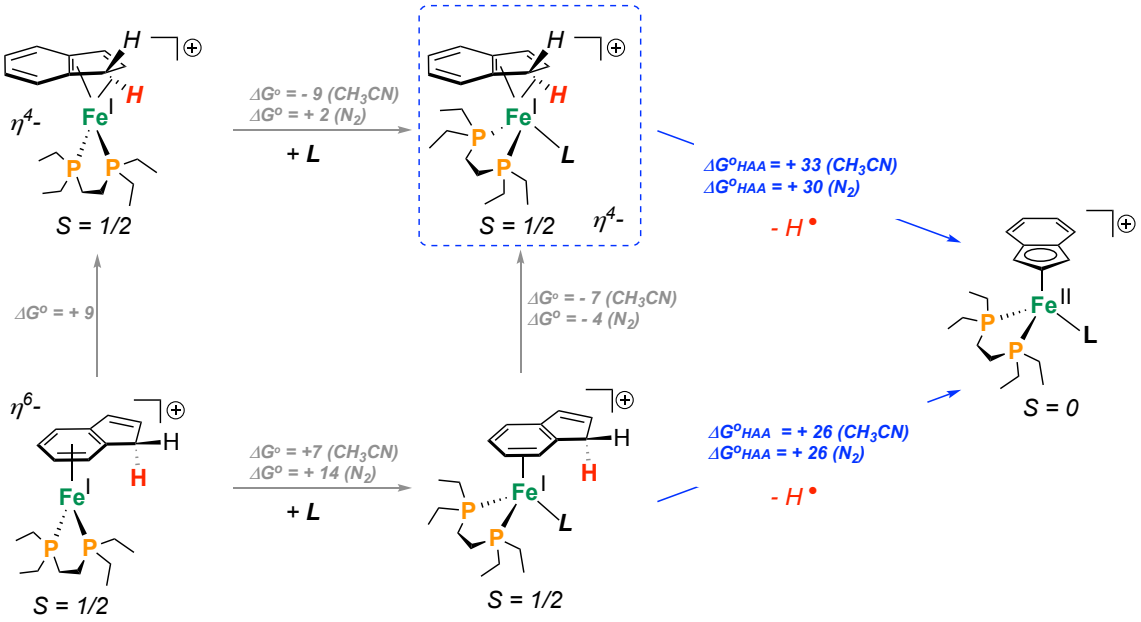

Table S4. Summary of DFT-calculated EPR parameters for [Fe^{III}Cp*(dppe)H]$^+$

Functional	Basis set	^{1}H (a_{iso}) (MHz)	^{1}H A (MHz)	^{1}H T (MHz)
experimental		36.7	[-10, 60, 60]	[-46.7, 23.3 23.3]
TPSSh	EPR-III (C & H) IGLO-III (P)	-66.34	[-19.33 -83.31 -85.15]	[43.23, -22.55, -20.67]
TPSSh	IGLO-III	-62.59	[-23.11, -88.89, 87.01]	[43.26, -20.72, -22.54]
TPSS	EPR-III (C & H) IGLO-III (P)	-42.33	[-3.85, -62.55, -60.59]	[38.48, -20.22, -18.26]
TPSS	IGLO-III	-39.72	[-1.21, -59.92, -58.02]	[38.51, -20.20, -18.30]
B3LYP	IGLO-III	-81.68	[-36.01, -105.51, -103.51]	[45.67, -23.83, -21.83]
BP86	IGLO-III	-34.39	[2.68, -54.06, -51.78]	[37.07, -19.67, -17.39]
M06l	IGLO-III	-49.08	[-4.69, -72.89, -69.67]	[44.39, -23.81, -20.59]

Table S5. Summary of DFT-calculated ^{57}Fe Mössbauer parameters

Compound	δ_{exp} **(mms^{-1})**	δ_{calc} **(mms^{-1})**	***ρ(0)*** **TPSSh+DKH**	$\lvert\Delta E_{Qexp}\rvert$ **(mms^{-1})**	$\lvert\Delta E_{Qcalc}\rvert$ **(mms^{-1})**	***Ref.***
Ferrocene	0.51	0.54	23598.91995	2.5	2.6	**16**
Ferrocenium	0.57	0.59	23598.94994	0	0.47	**16**
Fe(η^5-Cp)(dppe)(H)	0.26	0.33	23600.32909	1.91	1.86	**17**
[Fe(η^5-Cp*)(dppe)(H)]$^+$	0.26	0.33	23600.16782	0.84	1.10	**18**,**19**
Fe(η^3:η^2-Ind)(depe)(H) (**2**)	0.28	0.35	23600.02363	1.61	1.62	***this work***
[Fe(η^3:η^2-Ind)(depe)(H)]$^+$	--	0.33	23600.13298	--	0.90	***this work***
[Fe(η^6-IndH)(depe)]$^+$ ([**4**][BAr$^F{}_4$])	0.59	0.55	23598.90502	1.80	0.75	***this work***
[Fe(η^3:η^2-Ind)(depe)(PEt$_3$)]$^+$	--	0.36	23599.42829	--	1.72	***this work***
[Fe(η^3:η^2-Ind)(depe)(N$_2$)]$^+$	--	0.40	23599.72057	--	1.69	***this work***
[Fe(η^3:η^2-Ind)(depe)(H$_2$)]$^+$	--	0.40	23599.78043	--	1.65	***this work***
[Fe(η^3:η^2-Ind)(depe)(H)$_2$]$^+$	--	0.17	23601.04992	--	1.66	***this work***
[Fe(η^3:η^2-Ind)(depe)]$^+$ (S = 1)	--	0.55	23598.94974	--	1.35	***this work***
[Fe(η^6-C$_6$H$_5$CH$_3$)(dippe)]$^+$([**5**][BAr$^F{}_4$])	0.50	0.56	23598.82654	1.71	0.70	***this work***

Table S6. Mulliken atomic spin densities calculated for [Fe(η^3:η^2-Ind)(depe)(H)][$BAr^F{}_4$] ([**3**][$BAr^F{}_4$]). The red italicized atom corresponds to the hydride ligand with the value of $a_{iso}(^1H)$ provided to its right.

1	Fe	1.004222
2	P	-0.023195
3	P	-0.029529
4	C	0.049194
5	C	-0.041834
6	C	0.003854
7	C	0.075785
8	H	-0.003139
9	C	-0.047046
10	H	0.001708
11	C	0.002200
12	C	0.020057
13	H	-0.001148
14	C	0.004944
15	H	-0.000302
16	C	-0.037762
17	H	0.001462
18	C	0.003755
19	C	0.004541
20	H	0.002211
21	H	-0.000232
22	C	-0.042396
23	H	0.001438
24	C	0.000510
25	H	-0.000910
26	H	0.000278
27	C	0.002046
28	C	0.081118
29	H	-0.003645
30	C	0.000412
31	H	0.000098
32	H	0.000298
33	H	0.000009
34	C	0.000508
35	H	0.000364
36	H	-0.000094
37	H	0.000008
38	C	0.000560
39	H	-0.000002
40	H	-0.000152
41	H	-0.000484

42	C	-0.000034	
43	H	0.000031	
44	H	0.000339	
45	H	0.000035	
46	***H***	***-0.028443***	***$a_{iso}(^1H)$ = 40.4 MHz***
47	H	-0.001568	
48	H	0.000283	
49	H	0.000351	
50	H	-0.000554	
51	H	-0.000013	
52	H	-0.000248	
53	H	0.000445	
54	H	-0.000331	

Table S7. Mulliken atomic spin densities calculated for [Fe(η^6-IndH)(depe)][$BAr^F{}_4$] ([**4**][$BAr^F{}_4$]). The red italicized atoms correspond to the CH_2 moiety of the indene ligand with the value of $a_{iso}(^1H)$ provided to its right.

1	Fe	1.107057
2	C	-0.020525
3	C	-0.007300
4	C	0.030112
5	H	0.002934
6	C	0.005009
7	C	-0.013393
8	H	0.000614
9	C	0.008598
10	H	-0.000140
11	C	-0.014147
12	H	0.002396
13	C	-0.034156
14	H	0.002322
15	C	-0.002793
16	H	0.001041
17	P	-0.045210
18	P	-0.043973
19	C	0.000078
20	H	-0.000075
21	H	0.000442
22	H	0.000062
23	C	0.000278
24	H	0.000043
25	H	0.000802
26	H	0.000188

27	C	-0.002335	
28	H	0.000578	
29	H	0.000021	
30	C	-0.001156	
31	H	-0.000991	
32	H	-0.000082	
33	C	0.010649	
34	H	0.003180	
35	H	-0.000727	
36	C	0.001213	
37	H	-0.000028	
38	H	0.000390	
39	H	-0.000062	
40	C	0.000236	
41	H	0.000004	
42	H	0.000174	
43	H	-0.000123	
44	C	0.004419	
45	H	0.000103	
46	H	-0.001413	
47	C	0.008216	
48	H	0.000470	
49	H	-0.000183	
50	C	-0.000183	
51	H	-0.001390	
52	H	0.000085	
53	***H***	***-0.000061***	***$a_{iso}(^1H)$ = 0.087 MHz***
54	***H***	***-0.001270***	***$a_{iso}(^1H)$ = 1.80 MHz***

Table S8. Mulliken atomic spin densities calculated for [Fe(η^6-$C_6H_5CH_3$)(dippe)][BAr^F_4] ([**5**][BAr^F_4]). The red italicized atoms correspond to the toluene hydrogen atoms with the value of $a_{iso}(^1H)$ provided to its right.

1	Fe	1.109224	
2	P	-0.051012	
3	P	-0.045018	
4	C	0.008734	
5	***H***	***0.003451***	***$a_{iso}(^1H)$ = 4.90 MHz***
6	C	-0.000236	
7	H	0.000277	
8	H	0.000530	
9	H	0.000063	
10	C	0.001060	
11	C	0.012531	

12	H	0.000427	
13	C	-0.027437	
14	***H***	***0.001502***	***$a_{iso}(^1H)$ = 2.13 MHz***
15	C	0.000183	
16	H	-0.000005	
17	H	0.000301	
18	H	0.000008	
19	C	0.009207	
20	H	-0.000350	
21	C	-0.003332	
22	***H***	***0.001605***	***$a_{iso}(^1H)$ = 2.28 MHz***
23	C	-0.022314	
24	***H***	***0.001202***	***$a_{iso}(^1H)$ = 1.71 MHz***
25	C	0.000830	
26	H	0.000004	
27	H	-0.000220	
28	H	-0.000595	
29	C	-0.009873	
30	***H***	***0.001819***	***$a_{iso}(^1H)$ = 2.58 MHz***
31	C	0.000214	
32	H	-0.000003	
33	H	-0.000140	
34	H	0.000312	
35	C	0.005435	
36	H	-0.001251	
37	C	-0.000346	
38	H	0.000101	
39	H	0.000873	
40	H	0.000020	
41	C	-0.001815	
42	H	0.000681	
43	H	-0.000093	
44	C	0.002110	
45	H	-0.000682	
46	H	-0.000168	
47	H	0.000017	
48	C	0.002660	
49	***H***	***-0.000541***	***$a_{iso}(^1H)$ = -0.77 MHz***
50	***H***	***0.001438***	***$a_{iso}(^1H)$ = 2.04 MHz***
51	***H***	***-0.000513***	***$a_{iso}(^1H)$ = 0.73 MHz***
52	C	0.002485	
53	H	0.000163	
54	C	-0.002381	
55	H	-0.000963	
56	H	0.000033	

57	C	0.000474
58	H	0.000526
59	H	-0.000122
60	H	-0.000004
61	C	-0.000895
62	H	0.000069
63	H	-0.000299
64	H	0.000040

Figure S57. Spin density map of gas-phase optimized structures (isovalue: 0.004 *e*-/Å^3; TPSS functional: def2tzvp (Fe), def2svp (all other atoms).

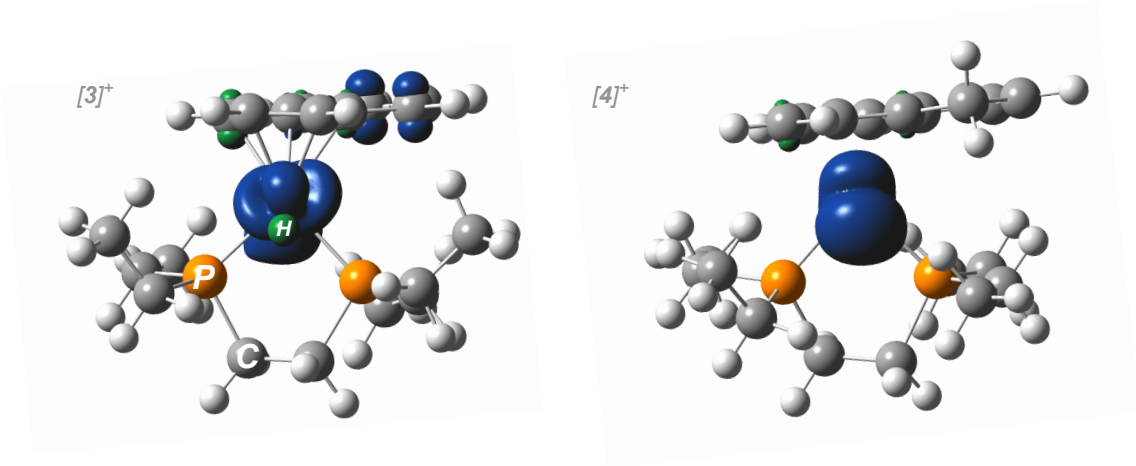

XIII. References:

[1] Mays, M. J.; Prater, B. E. *Inorg. Synth.* **1974**, *15*, 21.

[2] Hermes, A.R.; Girolami, G. S. *Organometallics* **1987**, *6*, 763.

[3] Hermes, A. R.; Warren. T. H.; Girolami, G. S. *J. Chem. Soc. Dalton Trans.* **1995**, 301.

[4] Hamon, P.; Toupet, L.; Hamon, J.R.; Lapinte, C. *Organometallics* **1992**, *11*, 1429.

[5] Prisecaru, I. *WMOSS4 Mössbauer Spectral Analysis Software, www.wmoss.org, 2009-2016.*

[6] Stoll, S.; Schweiger, A. *J. Magn. Reson*. **2006**, *178*, 42.

[7] Doyle, L. R.; Scott, D. J.; Hill, P. J.; Fraser, D. A. X.; Myers, W. K.; White, A. J. P.; Green, J. C.; Ashley, A. E. *Chem. Sci.* **2018**, *9*, 7362.

[8] Sheldrick, G. M.; IUCr. *Acta Crystallogr., Sect. A: Found. Crystallogr.* **2008**, *64*, 112.

[9] Dolomanov, O. V.; Bourhis, L. J.; Gildea, R. J.; Howard, J. A. K.; Puschmann, H. *J. Appl. Crystallogr.* **2009**, *42*, 339.

[10] Gaussian 09, Revision A.02, Frisch, M. J.; Trucks, G. W.; Schlegel, H. B.; Scuseria, G. E.; Robb, M. A.; Cheeseman, J. R.; Scalmani, G.; Barone, V.; Mennucci, B.; Petersson, G. A.; Nakatsuji, H.; Caricato, M.; Li, X.; Hratchian, H. P.; Izmaylov, A. F.; Bloino, J.; Zheng, G.; Sonnenberg, J. L.; Hada, M.; Ehara, M.; Toyota, K.; Fukuda, R.; Hasegawa, J.; Ishida, M.; Nakajima, T.; Honda, Y.; Kitao, O.; Nakai, H.; Vreven, T.; Montgomery, J. A., Jr; Peralta, J. E.; Ogliaro, F.; Bearpark, M. J.; Heyd, J.; Brothers, E. N.; Kudin, K. N.; Staroverov, V. N.; Kobayashi, R.; Normand, J.; Raghavachari, K.; Rendell, A. P.; Burant, J. C.; Iyengar, S. S.; Tomasi, J.; Cossi, M.; Rega, N.; Millam, N. J.; Klene, M.; Knox, J. E.; Cross, J. B.; Bakken, V.; Adamo, C.; Jaramillo, J.; Gomperts, R.; Stratmann, R. E.; Yazyev, O.; Austin, A. J.; Cammi, R.; Pomelli, C.; Ochterski, J. W.; Martin, R. L.; Morokuma, K.; Zakrzewski, V. G.; Voth, G. A.; Salvador, P.; Dannenberg, J. J.; Dapprich, S.; Daniels, A. D.; Farkas, Ö.; Foresman, J. B.; Ortiz, J. V.; Cioslowski, J.; Fox, D. J. Gaussian, Inc., Wallingford CT, 2016.

[11] Tao, J. M.; Perdew, J. P.; Staroverov, V. N.; Scuseria, G. E. *Phys. Rev. Lett.* **2003**, *91*, 146401.

[12] Weigend, F.; Ahlrichs, R. *Phys. Chem. Chem. Phys.* **2005**, *7*, 3297–3305.

[13] Matson, B. D.; Peters, J. C. *ACS Catal.* **2018**, *8*, 1448.

[14] Bjornsson, R.; Neese, F.; DeBeer, S. *Inorg. Chem.* **2017**, *56*, 1470.

[15] Römelt, M.; Ye, S.; Neese, F. *Inorg. Chem.* **2009**, *48*, 784.

[16] Malischewski, M.; Seppelt, K.; Sutter, J.; Munz, D.; Meyer, K. *Angew. Chem. Int. Ed.* **2018**, *57*, 14597.

[17] Patel, D.; Wooles, A.; Cornish, A.D.; Steven, L.; Davies, S.E.; Evans, D.J.; McMaster, J.; Lewis, W.; Blake, A.J.; Liddle, S.T. *Dalton Trans.* **2015**, *44*, 14159.

[18] Hamon, P.; Toupet, L.; Hamon, J.R.; Lapinte, C. *Organometallics* **1992**, *11*, 1429.

[19] Hamon, P.; Hamon, J.R.; Lapinte, C. *J. Chem. Soc., Chem. Commun.* **1992**, 1602.